

# Topological synchronization of quantum van der Pol oscillators

Christopher W. Wächtler<sup>1,2</sup> and Gloria Platero<sup>3</sup>

<sup>1</sup>*Max Planck Institut für Physik komplexer Systeme, 01187 Dresden, Germany*

<sup>2</sup>*Department of Physics, University of California, Berkeley, California 94720, USA*

<sup>3</sup>*Instituto de Ciencia de Materiales de Madrid, CSIC, Madrid 28049, Spain*

To observe synchronization in a large network of classical or quantum systems demands both excellent control of the interactions between the nodes and very accurate preparation of the initial conditions due to the involved nonlinearities and dissipation. This limits the applicability of this phenomenon for future devices. Here, we demonstrate a route towards significantly enhancing the robustness of synchronized behavior in open nonlinear systems that utilizes the power of topology. In a lattice of quantum van der Pol oscillators with topologically motivated couplings, boundary synchronization emerges in the classical mean field as well as the quantum model. In addition to its robustness against disorder and initial state perturbations, the observed dynamics is independent of the underlying topological insulator model provided the existence of zero-energy modes. Our work extends the notion of topology to the general nonlinear dynamics and open quantum system realm with applications to networks where specific nodes need special protection like power grids or quantum networks.

## I. INTRODUCTION

For many quantum mechanical applications dissipation is often regarded as an undesirable yet unavoidable consequence because it potentially degrades quantum coherences and renders the system classical. However, interactions with the environment can also be considered a fundamental resource for striking collective effects typically impossible in Hamiltonian systems. A hallmark of such collective behavior in nonequilibrium systems is the phenomenon of synchronization: in the complete absence of any time-dependent forcing from the outside, a group of oscillators adjusts their frequencies such that they spontaneously oscillate in unison [1, 2]. Synchronization is intimately related to the phenomenon of self-sustained oscillations, where a system maintains a periodic motion in an autonomous fashion [3–6]. In this sense, interactions with the environment and nonlinearities in the equations of motion represent prerequisites for synchronization.

Recently, synchronization has emerged in the quantum domain due to the developments in quantum technology which allow one to exquisitely tailor both the system and environmental properties. While for classical oscillators synchronization can be verified and characterized in terms of limit-cycle solutions in phase space, similar definitions for quantum systems remain challenging. This is primarily because the notion of phase space trajectories loses its meaning. Nevertheless, various different examples ranging from nonlinear oscillators to spin-1 systems and ensembles of atoms predict that synchronization survives down to the quantum regime [7–18].

In both quantum and classical systems, unavoidable imperfections – local deformations caused by ambient conditions as well as long-term degradation – have a significant impact on the collective behavior and can even destroy synchronicity altogether. Moreover, collective synchronized dynamics in large networks often sensitively depends on fine-tuned initial conditions. It is therefore desirable for a reliable performance of future devices to

identify universal principles to enhance the robustness of synchronization. In this work, we demonstrate that the power of topological phases of matter, which exhibit an unusual protection from the adverse effects of impurities [19–21] can be exploited for this task. Topological insulators describe a special class of solids exhibiting an insulating bulk but symmetry protected conducting surface states, known as topological edge states [22–25]. These edge states display a surprising immunity to a wide range of local deformations, inherently avoiding backscattering over broad energy ranges and even circumventing localization in the presence of disorder [26].

While the robustness of topological systems against imperfections is well established for isolated systems, it is a nontrivial problem to determine whether this feature is still available in open setups. Recently, the study of out-of-equilibrium systems has moved to the forefront of research in topological band structures, motivated largely by the desire to create interesting states of matter with properties beyond those achievable in equilibrium [27–35]. While topological band and bandgap structures are inherently tied to linear systems, we currently observe rapidly growing interest to generalize topological concepts to nonlinear systems, which in turn has sparked the field of nonlinear topological photonics and the phenomenon of topological lasing [36–41].

Despite these recent advancements, topology in nonlinear, out-of-equilibrium systems exhibiting synchronization phenomena is still largely unexplored in classical systems [42–44] and, to the best of our knowledge, missing entirely for quantum systems. Here, we systematically investigate the potential of this new field of *topological synchronization* for classical and quantum systems. In order to provide such a comprehensive study, we choose the van der Pol (vdP) oscillator [1, 2, 45] as our building block to construct topological lattices. Since the quantum version of the vdP oscillator [8, 9, 46, 47] reduces to its classical analog at the mean field level (specifically to the Stuart-Landau oscillator, which is the weakly nonlin-

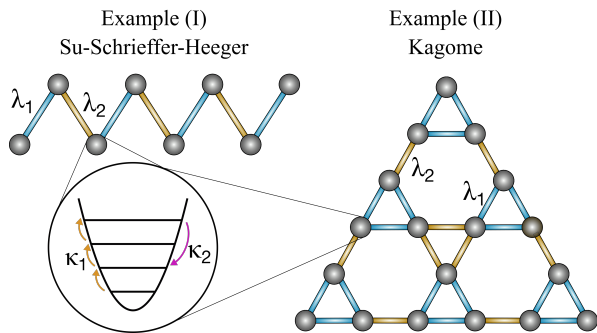


FIG. 1. The two topological lattices investigated in detail: Example (I) is the one-dimensional Su-Schrieffer-Heeger model and example (II) the breathing Kagome lattice. Both have alternating couplings  $\lambda_1$  and  $\lambda_2$  which give rise to topological edge or corner modes, respectively. In our model each lattice site consists of a quantum van der Pol oscillator, that is an harmonic oscillator driven out of equilibrium by two competing processes: one phonon gain with rate  $\kappa_1$  and two phonon loss with rate  $\kappa_2$ . The topologically motivated couplings give rise to symmetry-protected synchronization at the edges or corners of the respective lattices.

ear limit of the classical vdP oscillator), we are able to study the influence of topological band structures in both regimes. We show not only that boundary synchronization emerges in the classical as well as the quantum models if the underlying lattice possesses nontrivial topology, but also that it is protected over a wide range of local disorder. This effect is not specific to the considered examples of topological lattices in one and two dimensions but occurs in any topological insulator model as long as it exhibit zero-energy midgap states. More broadly, our results pave the way toward utilizing topology as a powerful tool for enhancing the robustness of collective dynamics in nonlinear open quantum systems.

*Outline:* The rest of this paper is laid out as follows. In Sec. II we discuss our proposed theoretical model to investigate the interplay of topology and synchronization in a network of quantum vdP oscillators, which includes an introduction to synchronization and the quantum vdP oscillator in Sec. II A and the full quantum model in Sec. II B. The mean field description of our model is provided in Sec. II C followed by its quantum fluctuations in Sec. II D. In the next Sec. III we present our numerical results: First we provide some general comments in Sec. III A followed by the two specific examples (shown in Fig. 1) of the Su-Schrieffer Heeger (SSH) model in Sec. III B and the breathing Kagome lattice in Sec. III C. Afterwards, we discuss our findings in Sec. IV. Finally, we propose possible experimental realizations in Sec. V and conclude in Sec. VI.

## II. THEORETICAL DESCRIPTION OF TOPOLOGICAL SYNCHRONIZATION

### A. Synchronization and the quantum van der Pol oscillator

Before we introduce the full model of coupled quantum vdP oscillators on a topological lattice, let us summarize some essential concepts of synchronization, which will also help us to clarify the notions we use throughout this work. A key component for synchronization are self-sustained oscillations, which describe periodic motion driven by a source of power that lacks a corresponding periodicity (in contrast to resonance phenomena) [3]. Importantly, after perturbation of their oscillation, autonomous systems restore their original rhythm. In phase space such dynamics will appear as a closed orbit known as limit cycle, and trajectories in the vicinity of this orbit are attracted towards it. A paradigmatic model exhibiting such self-sustained oscillations is the Stuart-Landau oscillator – the weakly nonlinear limit of the vdP oscillator – which describes the dynamics of a complex amplitude  $\alpha(t) \in \mathbb{C}$  with frequency  $\omega_0$  subject to negative and nonlinear damping:

$$\dot{\alpha} = -i\omega_0\alpha + \frac{\kappa_1}{2}\kappa_1 - \kappa_2|\alpha|^2\alpha. \quad (1)$$

Here, the rates  $\kappa_1$  and  $\kappa_2$  are assumed to be positive. The trivial solution  $\alpha(t) = 0$ , which is a fixed point of the right hand side of Eq. (1), is unstable as any small perturbation results in trajectories leading away from the origin in the complex plane. By contrast,  $\bar{\alpha}(t) = A_0 \exp(-i\omega_0 t + \varphi)$  with  $A_0 = \sqrt{\kappa_1/2\kappa_2}$  and arbitrary phase  $\varphi$  is a stable periodic solution with closed orbits in phase space.

Suppose that two of these Stuart-Landau oscillators  $\alpha_j$  and  $\alpha_{j'}$  with different frequencies are coupled. Due to their mutual interaction they may adjust their rhythms to oscillate with a common frequency, which as been described as ‘the essence of synchronization’ [1]. Depending on the initial conditions as well as the coupling strengths they will oscillate in perfect unison or with a fixed phase difference such that

$$\frac{d}{dt}\Delta\varphi_{jj'} = \frac{d}{dt}(\varphi_j - \varphi_{j'}) = 0. \quad (2)$$

Throughout this work we will refer to two classical systems being synchronized if Eq. (2) is fulfilled, which is less strict than other definitions, where synchronization is defined as  $\Delta\varphi_{jj'} = 0$  [1, 2].

Recently, it has been realized that a quantum harmonic oscillator subject to one-phonon gain and two-phonon loss fulfills Eq. (1) within a mean field approximation, which has inspired the term *quantum van der Pol oscillator* [8, 9, 46, 47] (far less common quantum Stuart-Landau oscillator [48]). In an open quantum system approach [49, 50] and using the notation  $\mathcal{D}[O]\varrho = O\varrho O^\dagger - \frac{1}{2}\{O^\dagger O, \varrho\}$ , the dynamics of the system density matrix  $\varrho(t)$  of this model is described by the

master equation

$$\dot{\varrho} = -\frac{i}{\hbar} [\omega_0 a^\dagger a, \varrho] + \kappa_1 \mathcal{D}[a^\dagger] \varrho + \kappa_2 \mathcal{D}[a^2] \varrho, \quad (3)$$

where  $a^\dagger$  ( $a$ ) is a bosonic creation (annihilation) operator. Furthermore,  $\kappa_1$  and  $\kappa_2$  denote the rates analogous to negative and nonlinear damping of the classical model, respectively. The classical equation of motion [cf. Eq. (1)] is recovered for the expectation value  $\alpha = \langle a \rangle \in \mathbb{C}$  by strictly factorizing all expectation values (mean field approximation).

Similar to the classical model, one may couple two or more of these quantum vdP oscillators and search for signatures of synchronization [8, 47]. However, generalizing the previously introduced notions of synchronization is challenging as phase space trajectories are ill defined concepts in the quantum regime. To overcome this challenge, synchronization measures in terms of the Husimi-Q or Wigner phase space distributions [8, 11, 51], explicit limit cycles of system observables [52, 53], or information-theoretical measures [54, 55] have been proposed. In this work, we use a measure to quantify synchronization of two quantum systems  $j$  and  $j'$  that is based on their dimensionless quadratures as [56]

$$S_c(j, j') = \langle (X_{2j-1} - X_{2j'-1})^2 + (X_{2j} - X_{2j'})^2 \rangle^{-1} \leq \frac{1}{4}, \quad (4)$$

where  $X_{2j-1} = (a_j + a_j^\dagger)/\sqrt{2}$  and  $X_{2j} = -i(a_j - a_j^\dagger)/\sqrt{2}$ . The upper bound of the quantum synchronization measure arises from the Heisenberg uncertainty principle. As  $S_c(j, j')$  may exhibit oscillations even in the long time limit, we perform time averages of this quantity, i.e.,

$$\langle S_c(j, j') \rangle = \frac{1}{t_f - t_i} \int_{t_i}^{t_f} S_c(j, j') dt'. \quad (5)$$

with initial time  $t_i$  and final time  $t_f$ . Throughout this work we are interested in the (periodic) steady state dynamics and discard transient dynamics, such that both  $t_i$  and  $t_f$  are taken to be larger than the transient relaxation time (see also Sec. III A).

### B. Van der Pol oscillator network as a quantum simulator of a topological lattice

Our model is formed by a lattice of  $N$  sites, each consisting of a quantum vdP oscillator labeled by the index  $j = 1, \dots, N$  and we assume identical oscillators with frequency  $\omega_0$ . The Hamiltonian of the system can be written as a tight-binding Hamiltonian

$$H = H_0 + H_{\text{top}} = \hbar \sum_j \omega_0 a_j^\dagger a_j + \hbar \sum_j \sum_{j' \neq j} \lambda_{jj'} (a_j^\dagger a_{j'} + a_j a_{j'}^\dagger), \quad (6)$$

where  $a_j^\dagger$  ( $a_j$ ) denote creation (annihilation) operators of bosonic particles at lattice site  $j$ . This general form

of the system Hamiltonian allows us to realize different topological lattice models simply by modifying the couplings  $\lambda_{jj'}$ . The dynamics of the system density matrix  $\varrho(t)$  is described by the master equation

$$\dot{\varrho} = -\frac{i}{\hbar} [H, \varrho] + \sum_j \{ \kappa_1 \mathcal{D}[a_j^\dagger] \varrho + \kappa_2 \mathcal{D}[a_j^2] \varrho \}. \quad (7)$$

Throughout this work we focus on the weak dissipation regime, that is we assume that  $\kappa_1, \kappa_2 \ll \omega_0$ . For realistic systems, this regime corresponds to long coherence times and weak coupling to the reservoirs such that a description of the system dynamics in terms of a Lindblad master equation [cf. Eq. (7)] is valid. Furthermore, we are interested in the limit which corresponds to large  $\kappa_2$  compared to  $\kappa_1$  as in this case each oscillator remains close to its ground state [8].

### C. Mean field model

From the full quantum model defined in Eq. (7), one may derive classical equations of motion for the expectation values  $\alpha_j = \langle a_j \rangle \in \mathbb{C}$  by performing a mean field approximation [cf. Sec. II A]. The governing equation of the complex-valued mean field amplitudes  $\alpha = (\alpha_1, \dots, \alpha_N)$  is then given by

$$\dot{\alpha} = -\frac{i}{\hbar} \underline{H} \alpha + \frac{\kappa_1}{2} \alpha - \kappa_2 (\alpha \odot \alpha^* \odot \alpha), \quad (8)$$

where  $\underline{H} = \underline{H}_0 + \underline{H}_{\text{top}}$  denotes the matrix corresponding to the Hamiltonian  $H$  [cf. Eq. (6)] with diagonal matrix  $\underline{H}_0 = \hbar \omega_0 \underline{1}$  and the matrix describing the coupling between oscillators  $\underline{H}_{\text{top}}$ . Furthermore,  $\odot$  denotes the Hadamard product defined as  $(\underline{F} \odot \underline{G})_{mn} = \underline{F}_{mn} \cdot \underline{G}_{mn}$  for two matrices  $\underline{F}$  and  $\underline{G}$ .

In the absence of any coupling between the oscillators ( $\lambda_{jj'} \equiv 0$ ) each oscillator will approach its respective periodic steady state [cf. Sec. II A]. For  $\kappa_2 > \kappa_1$  we expect small oscillation amplitudes which remain close to the fixed point  $\alpha_{\text{FP}} \equiv \mathbf{0}$  even if the coupling  $\lambda_{jj'}$  is comparable to the intrinsic frequency  $\omega_0$ . Consequently, we turn to the concept of linear stability (LS) analysis, which has proven to be useful to investigate the emergence of synchronized periodic motion in nonlinear systems [2]. To this end, we linearize Eq. (8) around the fixed point  $\alpha_{\text{FP}}$ ,

$$\dot{\alpha} = \alpha_{\text{FP}} + \underline{J}(\alpha - \alpha_{\text{FP}}) + \mathcal{O}(\alpha_{\text{FP}}^2) = \underline{J}\alpha + \mathcal{O}(\alpha_{\text{FP}}^2), \quad (9)$$

where the Jacobian matrix  $\underline{J}$  with entries  $J_{jj'} = \partial \dot{\alpha}_j / \partial \alpha_{j'}$  is evaluated at the fixed point resulting in the matrix

$$\underline{J} = -\frac{i}{\hbar} \underline{H} + \frac{\kappa_1}{2} \underline{1} = -\frac{i}{\hbar} (\underline{H}_0 + \underline{H}_{\text{top}}) + \frac{\kappa_1}{2} \underline{1}. \quad (10)$$

Since  $\underline{H}_{\text{top}}$  is a Hermitian matrix, it has real eigenvalues  $\hbar \mu^{(l)}$ , where  $l = 1, \dots, N$  is an index for the different eigenvalues. Moreover, the diagonal entries of  $\underline{J}$  are given

by  $-i\omega_0 + \kappa_1/2$ , such that  $\nu^{(l)} = -i(\omega_0 + \mu^{(l)}) + \kappa_1/2$  will be the eigenvalues of  $\underline{J}$ .

The spectrum of  $\underline{J}$  reveals information about the stability of the fixed point  $\alpha_{\text{FP}}$  and the overall dynamics near this fixed point: As long as the real parts of all eigenvalues are negative ( $\kappa_1 < 0$ ), the fixed point is stable and thus attracts all neighboring trajectories. As a result, there are no self-sustained oscillations. However, if the real part of one eigenvalue becomes positive, as we assume throughout this work ( $\kappa_1 > 0$ ), the fixed point becomes unstable and instead stable limit cycles emerge.

As mentioned previously, for  $\kappa_2 > \kappa_1$  the emerging limit cycles remain close to the fixed point. Consequently, the dynamics of the oscillator lattice (after relaxation) is well approximated by a superposition of eigenvectors,

$$\alpha_{\text{LS}}(t) = \sum_l c^{(l)} \alpha^{(l)} e^{-i[\omega_0 + \mu^{(l)}]t}, \quad (11)$$

where  $\mu^{(l)}$  and  $\alpha^{(l)}$  are the eigenvalues and their respective eigenvectors of  $\underline{H}_{\text{top}}/\hbar$ , and  $c^{(l)}$  denotes scalar coefficients.

#### D. Quantum fluctuations

To unravel quantum signatures beyond the mean field amplitudes  $\alpha_j$ , our aim is to find an approximate solution to the full quantum master Eq. (7). The fluctuations about these mean fields determined from the classical nonlinear equations of motions [cf. Eq. (8)] will be treated in a linearized model as Gaussian noise. This is done by moving to a displaced frame via the displacement operator

$$D[\alpha(t)] = \exp \left\{ \sum_j [\alpha_j(t) a_j - \alpha_j^*(t) a_j^\dagger] \right\} \quad (12)$$

and defining the density matrix in the displaced frame as  $\varrho_\alpha(t) = D^\dagger[\alpha(t)] \varrho(t) D[\alpha(t)]$  [48, 57]. By neglecting terms of order  $\mathcal{O}(a_j^3)$  and higher as detailed in App. A, we obtain an effective master equation of Lindblad form governing the dynamics of the fluctuations about the mean field amplitudes,

$$\dot{\varrho}_\alpha = -\frac{i}{\hbar} [H_\alpha, \varrho_\alpha] + \sum_j \left\{ \kappa_1 \mathcal{D}[a_j^\dagger] \varrho_\alpha + 4\kappa_2 |\alpha_j|^2 \mathcal{D}[a_j] \varrho_\alpha \right\} \quad (13)$$

with effective (squeezing) Hamiltonian

$$H_\alpha = H - i\hbar \frac{\kappa_2}{2} \sum_j [\alpha_j^2 (a_j^\dagger)^2 - (\alpha_j^*)^2 a_j^2]. \quad (14)$$

Notably, the mean field amplitudes  $\alpha_j$  appearing in Eqs. (13) and (14) satisfy the dynamics governed by Eq. (8).

As the Hamiltonian (14) is quadratic, the dynamics of the effective quantum model is fully described by the covariance matrix  $\underline{C}_{mn} = \text{Tr}[\varrho_\alpha \{X_m, X_n\}/2]$  with the

quadratures  $X_{2j-1} = (a_j + a_j^\dagger)/\sqrt{2}$  and  $X_{2j} = -i(a_j - a_j^\dagger)/\sqrt{2}$ . The equation of motion of the covariance matrix  $\underline{C}$  is given by [58]

$$\dot{\underline{C}} = \underline{B} \underline{C} + \underline{C} \underline{B}^\top + \underline{D}, \quad (15)$$

where  $\underline{B}$  and  $\underline{D}$  are determined from Eq. (13); see App. B. Throughout this work, we consider a pure coherent state as the initial state of the density matrix  $\varrho(0) = \bigotimes_j |\alpha_j(0)\rangle \langle \alpha_j(0)|$ . In the comoving frame, such an initial condition corresponds to  $\varrho_\alpha(0) = \bigotimes_j |0_j\rangle \langle 0_j|$  which results in an initial covariance matrix of diagonal form, i.e.,  $\underline{C}(0) = 1/2 \cdot \underline{1}$ , which reflects the Heisenberg uncertainty principle. Note that through the covariance matrix  $\underline{C}$  we have direct access to the quantum synchronization measure of Eq. (4).

### III. RESULTS

#### A. Preliminary remarks

Before we turn to the detailed analysis of two specific topological lattices in the next two sections, we would like to provide some general notions that will apply to both examples in order to minimize redundancies. Within each section,  $\alpha^{(l)}$  indicates an eigenstate with eigenvalue  $\hbar\mu^{(l)}$  of the respective topological (coupling) Hamiltonian, i.e.,  $H_{\text{SSH}}$  in Sec. III B and  $H_{\text{Kag}}$  in Sec. III C. Furthermore, the mean field amplitude of lattice site  $j$  is denoted by  $A_j(t)$  and defined via  $A_j(t) = [\alpha_j(t) + \alpha_j^*(t)]/2$ . Throughout, when random initial conditions are considered, we mean randomly distributed complex amplitudes and phases, i.e.,  $a_j(t=0) = \alpha_j^r \exp(i\varphi_j^r)$  where  $\alpha_j^r$  and  $\varphi_j^r$  are random variables chosen from the uniform distributions  $\alpha_j^r \sim \mathcal{U}(0, 0.5)$  and  $\varphi_j^r \sim \mathcal{U}(0, 2\pi)$ , respectively. Similarly, when random disorder with strength  $r$  is applied to the coupling between lattice sites  $j$  and  $j'$  we refer to  $\lambda_{jj'} \rightarrow \lambda_{jj'} + \delta\lambda_{jj'}^r$  with  $\delta\lambda_{jj'}^r \sim \mathcal{U}(-r, r)$ . Lastly, all numerical results shown are obtained after a significant relaxation time  $\omega_0 t_{\text{rel}} = 2 \cdot 10^4$  in order to discard transient effects.

#### B. Example (I): Topological synchronization in the one-dimensional SSH chain

##### 1. The SSH model

In the following we investigate the interplay of topology and synchronization in the paradigmatic SSH model, a one-dimensional dimerized lattice with staggered nearest-neighbor hopping and time reversal, particle-hole and chiral symmetry (BDI class); a sketch is shown in Fig. 1. Recently, implementations of this model under nonequilibrium conditions or in strongly nonlinear systems have been proposed [59–63] and experimentally realized [64]. Here, we briefly summarize some key results needed

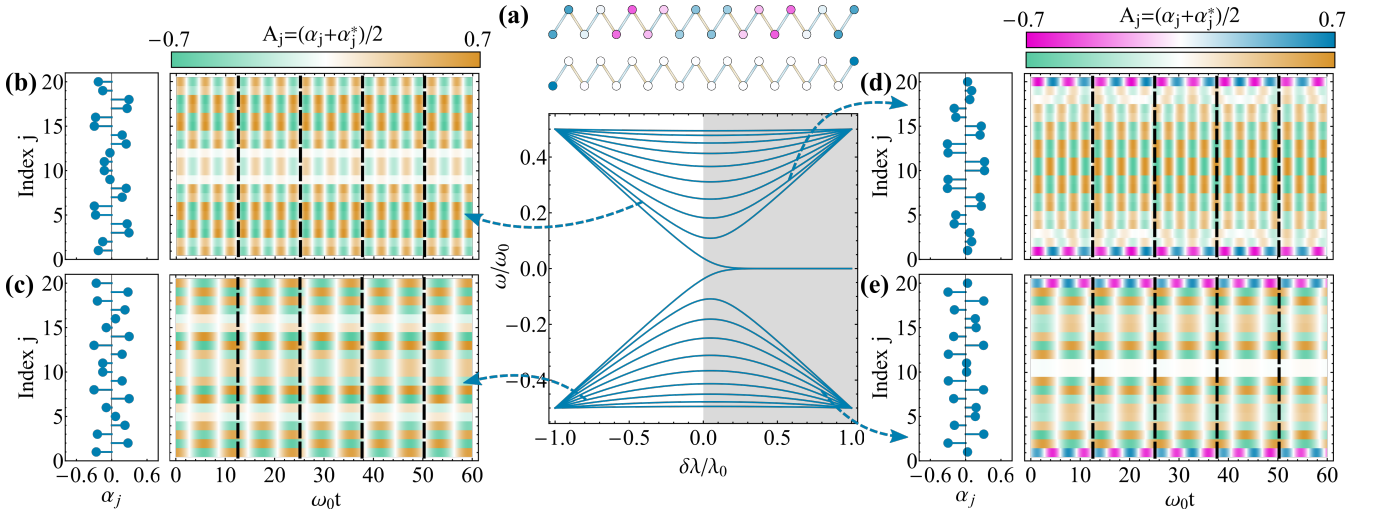


FIG. 2. (a) Eigenspectrum of  $H_{\text{SSH}}$  (or equivalently  $\underline{H}_{\text{SSH}}$ ) for  $N = 20$  with  $\lambda_1 = \lambda_0 - \delta\lambda$  and  $\lambda_2 = \lambda_0 + \delta\lambda$ , where the gray region marks the topological phase ( $\lambda_2 > \lambda_1$ ). The top two lattices show examples of a delocalized bulk state (top) and a highly localized edge state (bottom) for  $\delta\lambda/\lambda_0 = 0.8$ . (b)–(e) Left panels show the amplitudes  $\alpha_j^{(l)}$  of the eigenvectors corresponding to the eigenvalues  $\hbar\mu^{(l)}$  marked by the blue arrows of the eigenspectrum (a), specifically (b)  $\mu^{(l)} = 0.94\lambda_0$  for  $\delta\lambda/\lambda_0 = -0.4$ , (c)  $\mu^{(l)} = -1.89\lambda_0$  for  $\delta\lambda/\lambda_0 = -0.8$ , (d)  $\mu^{(l)} = 1.23\lambda_0$  for  $\delta\lambda/\lambda_0 = 0.6$ , and (e)  $\mu^{(l)} = -1.87\lambda_0$  for  $\delta\lambda/\lambda_0 = 0.8$ . These eigenstates are the initial states for the mean field dynamics of the vdP network. The amplitude dynamics  $A_j(t)$  of each oscillator  $j$  is shown in the right panels. In the nontrivial topological phase [panels (d) and (e)] the two oscillators located at the edges ( $j = 1$  and  $j = 20$ ) are highlighted in blue/pink. Parameters:  $\kappa_1 = 5 \cdot 10^{-3} \omega_0$ ,  $\kappa_2 = 2\kappa_1$ ,  $\lambda_0 = 0.25\omega_0$ .

to understand its topological character and refer to Refs. [65–67] for further details. The Hamiltonian of the model is given by

$$H_{\text{SSH}} = \hbar \sum_j \lambda_j (a_j^\dagger a_{j+1} + a_{j+1}^\dagger a_j), \quad (16)$$

where  $\lambda_j = \lambda_1$  if  $j$  is odd and  $\lambda_j = \lambda_2$  otherwise. The spectrum of the Hamiltonian (16) is symmetric with respect to the zero-energy axis ( $E = 0$ ) as a result of the chiral symmetry present in the system. The symmetry relation reads

$$\Gamma H_{\text{SSH}} \Gamma = -H_{\text{SSH}} \quad (17)$$

with  $\Gamma = \exp\{i\frac{\pi}{2} \sum_j [1 - (-1)^j] a_j^\dagger a_j\}$ . After considering the bulk Hamiltonian, assuming periodic boundary conditions,

$$\tilde{H}_{\text{SSH}}(k) = \hbar \begin{pmatrix} 0 & \lambda_1 + \lambda_2 e^{ik} \\ \lambda_1 + \lambda_2 e^{-ik} & 0 \end{pmatrix}, \quad (18)$$

we observe that the system consists of two dispersive bands separated by a gap. At  $\lambda_1 = \lambda_2$ , i.e., in the absence of dimerization, this band gap closes (at  $k = \pm\pi$ ) and a phase transition occurs. This phase transition is of topological nature and separates the trivial phase ( $\lambda_1 > \lambda_2$ ) from the topological phase ( $\lambda_1 < \lambda_2$ ). In Fig. 2(a) we show the eigenspectrum of  $H_{\text{SSH}}$  for  $N = 20$  lattice sites as a function of  $\delta\lambda$ , where  $\lambda_1 = \lambda_0 - \delta\lambda$  and  $\lambda_2 = \lambda_0 + \delta\lambda$ . For the chain with finite length eigenvectors within the

bands are delocalized along the whole chain; an example is shown in the top lattice of Fig. 2(a) and in the left panels of Figs. 2(b)–(e).

In addition, two degenerate zero-energy states occur within the band gap in the topological phase ( $\delta\lambda > 0$ ), which are highly localized at the boundaries of the system; an example is shown in the bottom lattice of Fig. 2(a). The edge states are topologically protected by the chiral symmetry and are thus robust against (symmetry-preserving) local perturbations as we discuss in more detail below.

## 2. Topological effects on synchronization at the mean field level

To incorporate the topological character of the SSH model into the network of vdP oscillators, the coupling matrix  $\underline{H}_{\text{top}}$  in Eq. (8) is chosen to be  $\underline{H}_{\text{SSH}}$ . In the following we compare the numerical results to our analytic considerations of Sec. II C. In the right panels of Figs. 2(b)–(e) we show the amplitude dynamics  $A_j(t)$  of the oscillator at site  $j$  when an eigenstate  $\alpha^{(l)}$  of  $\underline{H}_{\text{SSH}}$  is chosen as initial state, shown in blue in the left panels of Figs. 2(b)–(e).

We start our discussion in the trivial phase ( $\delta\lambda < 0$ ). In Figs. 2(b) and (c), we observe complete synchronization, i.e. all lattice sites  $j$  oscillate with the same frequency  $\omega_0 + \mu^{(l)}$ . This frequency is determined by the choice of initial eigenstate  $\alpha^{(l)}$  with respective eigen-

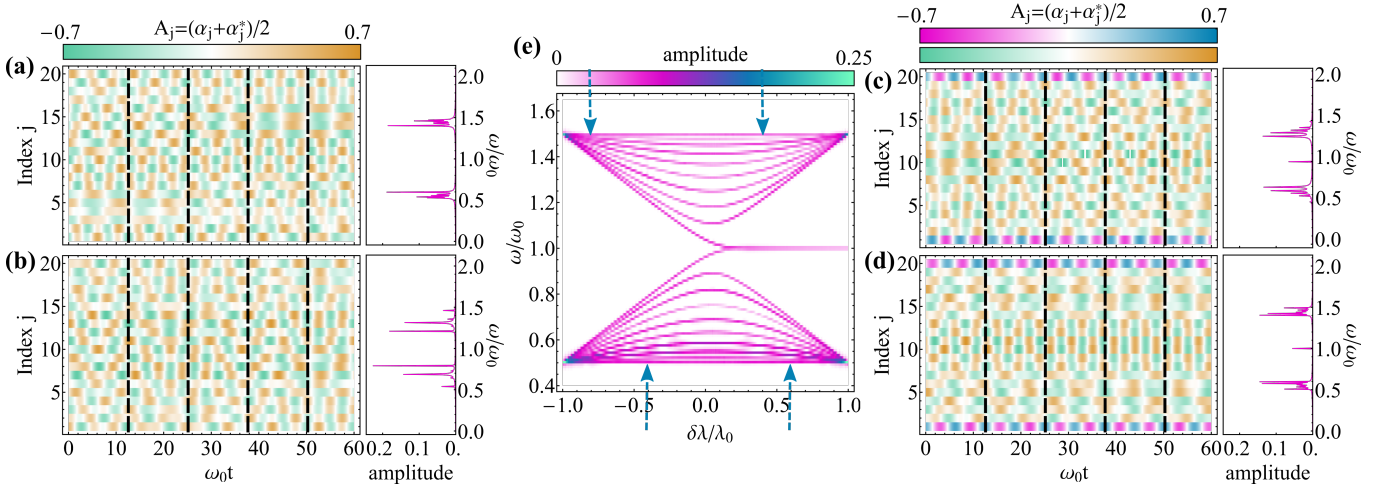


FIG. 3. (a)–(d) Left panels show the amplitude dynamics  $A_j(t)$  of each oscillator  $j$  of the vdP network for random initial conditions for different couplings (a)  $\delta\lambda = -0.8\lambda_0$ , (b)  $\delta\lambda = -0.4\lambda_0$ , (c)  $\delta\lambda = 0.4\lambda_0$ , and (d)  $\delta\lambda = 0.6\lambda_0$  [also marked with blue arrows in panel (e)]. The two oscillators located at the edges ( $j = 1$  and  $j = 20$ ) are highlighted in blue/pink in panels (c) and (d). Right panels show the frequency spectrum obtained from a discrete Fourier transform of the dynamics of the left panels. (e) Reconstruction of the eigenspectrum of  $H_{SSH}$  (or equivalently  $\underline{H}_{SSH}$ ) from the oscillation dynamics averaged over 10 realizations of random initial conditions. Parameters:  $\kappa_1 = 5 \cdot 10^{-3}\omega_0$ ,  $\kappa_2 = 2\kappa_1$ ,  $\lambda_0 = 0.25\omega_0$ .

value  $\hbar\mu^{(l)}$ . Hence, the oscillation frequency in panel (b) [(c)] is larger (smaller) compared to the intrinsic frequency  $\omega_0$  of the uncoupled vdP oscillators. Furthermore, the amplitude of the initial state  $\alpha_j^{(l)}$  directly translates to the oscillation amplitudes  $A_j(t)$  and their phases. Thus in accordance to our previous analytic considerations the dynamics in the trivial phase is given by  $\alpha(t) = c\alpha^{(l)} \exp\{-i[\omega_0 + \mu^{(l)}]t\}$  with a scaling factor  $c$ .

For  $\delta\lambda > 0$ , however, nontrivial topological effects on the dynamics of the lattice emerge as shown in Figs. 2(d) and (e): Even though the initial bulk eigenstate (shown in the left panels) exhibits only small amplitudes at the edges ( $j = 1$  and  $j = 20$ ) the oscillation amplitudes (highlighted in blue/pink) are comparable to the largest amplitudes in the whole chain. Moreover, they oscillate with the intrinsic frequency  $\omega_0$  (the vertical dashed lines are located at integer multiples of  $\omega_0 t = 4\pi n$ ,  $n \in \mathbb{N}$ ). In comparison to the trivial phase, where small initial amplitudes remain small for all lattice site, the edge modes in the topological phase are always excited. Note that the edge states are not strictly localized at the two boundary lattice sites, but rather extend exponentially into the bulk. Consequently, the dynamics of bulk oscillators close to the edge, e.g.  $j = 3$  or  $j = 18$ , is a superposition of the initial state and the edge state with different frequencies. Thus, the dynamics of these oscillators is given by  $\alpha_j(t) \propto \alpha_j^{(l)} \exp\{-i[\omega_0 + \mu^{(l)}]t\} + \alpha_j^{edge} \exp(-i\omega_0 t)$ , where  $\alpha_j^{(l)}$  and  $\alpha_j^{edge}$  represent the initial and edge eigenstate.

Since it might be difficult in an experimental setup to initiate the system in a specific eigenstate  $\alpha^{(l)}$  of  $\underline{H}_{SSH}$ , the question arises how a randomly distributed initial state affects the dynamics and whether the previously

discussed zero-energy edge mode synchronization persists in such a scenario. To this end, we show in the left panels of Figs. 3(a)–(d) the amplitude dynamics  $A_j(t)$  for such random initial states (cf. Sec. III A). In the trivial phase shown in panels (a) and (b) there is no clear pattern of synchronization. We would like to note that some oscillators in Figs. 3(a) and (b) might be synchronized for short times, however, their phase difference is not constant over longer times (see Sec. II A).

In order to confirm our intuition that there are many frequencies participating in the dynamics of the vdP network, we perform a discrete Fourier transform and show the frequency spectrum in the right panels of Figs. 3(a) and (b). As expected there are multiple peaks centered around  $\omega_0$  and separated by a gap. These peaks correspond to the eigenfrequencies  $\omega_0 + \mu^{(l)}$  of the system.

In the topological phase shown in Figs. 3(c) and (d) the oscillator dynamics (left panels) is similar to the one described previously for the trivial phase. However, there is an important difference: The edges (highlighted in blue/pink) do not exhibit frequency mixing but oscillate with one specific frequency, the intrinsic frequency  $\omega_0$ . Hence, the edges are synchronized with one another, yet due to the random initial conditions with a possible phase shift (e.g. different amplitudes at the dashed lines for  $j = 1$  and  $j = 20$ ). However, the phase difference remains constant over time. In the frequency spectrum of the discrete Fourier analysis, we observe now an additional sharp peak at  $\omega = \omega_0$  confirming the existence of the synchronized edge modes.

In terms of the discrete Fourier analysis we are able to analyze the full spectrum of the coupling matrix  $\underline{H}_{SSH}$  for random initial conditions. In Fig. 3(e) we show the

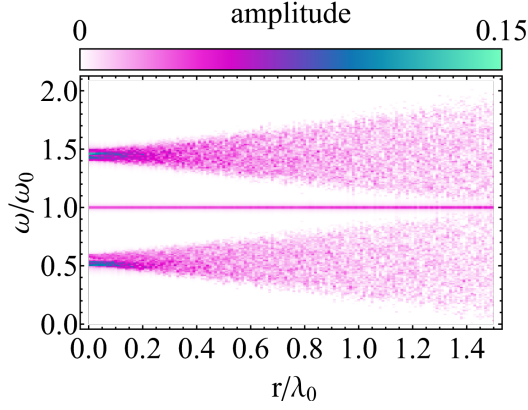


FIG. 4. Frequency spectrum of the vdP network for  $\delta\lambda = 0.8\lambda_0$  obtained via discrete Fourier transformation as a function of the disorder strength  $r$ . Disorder is applied to the couplings between neighboring sites via local perturbations uniformly distributed over the interval  $(-r, r)$ . While the band frequencies are strongly affected by the disorder, the edge modes located at  $\omega = \omega_0$  are robust, even for large amounts of disorder. Parameters:  $\kappa_1 = 5 \cdot 10^{-3}\omega_0$ ,  $\kappa_2 = 2\kappa_1$ ,  $\lambda_0 = 0.25\omega_0$ , 10 realizations of random initial states for each value of  $r$ .

result of the frequency spectrum averaged over 10 realizations of random initial conditions as a function of  $\delta\lambda$ . Remarkably, the spectrum is identical to the eigenspectrum of  $\underline{H}_{\text{SSH}}$ , which confirms that the synchronized edge modes are only present in the topological phase ( $\delta\lambda > 0$ ).

One of the hallmarks of topological insulators is that they exhibit extremely robust surface states since no local perturbation can change their global topology. For the SSH model the robustness arises from an underlying chiral symmetry. To test whether this extraordinary feature is also present in our open nonlinear system of vdP oscillators, we apply random disorder to the couplings between neighboring sites [cf. Eq. (16) and Sec. II A]. In Fig. 4 we show the frequency spectrum of the discrete Fourier analysis for the coupling  $\delta\lambda = 0.8t_0$  as a function of the disorder strength  $r$  for 10 realizations. While the frequencies within the upper and lower band spread over a wide range as the disorder strength is increased, the edge mode persists even for disorders as large as  $r = 1.5\lambda_0$  before the bands start overlapping with the zero energy mode.

### 3. Quantum signatures of topological synchronization

In the previous section the focus has been the effects of topology on the mean field dynamics. Thus, the observed signatures are classical in nature even though the underlying model is quantum. By contrast, in this section we analyze the quantum fluctuations about the mean field amplitudes and investigate whether a similar interplay of topology and synchronization carries on beyond the mean field level. To this end, we use the measure

$\langle S_c(j, j') \rangle$  [cf. Eq. (5)] to quantify quantum synchronization between two lattice sites  $j$  and  $j'$ . For the effective quantum model [cf. Eq. (13)–(14)] this measure can be calculated via the covariance matrix  $\underline{C}$  and we use throughout this section the mean field amplitudes after relaxation as initial conditions. We focus here on the case of random initial conditions, that is the quantum fluctuations corresponding to the mean field dynamics shown in Figs. 3(a)–(d). In this way we are able to highlight the topological signatures while keeping the discussion precise. Furthermore, as we show in App. C, the significant results that occur for random initial conditions also carry on if eigenstates  $\alpha^{(l)}$  are chosen as initial conditions (similar as to the topological effects observed in the mean field dynamics; cf. Sec. III B 2).

In Figs. 5(a)–(d) we show the time-averaged quantum synchronization measure  $\langle S_c(j, j') \rangle$  for different couplings strengths (a)  $\delta\lambda = -0.8\lambda_0$ , (b)  $\delta\lambda = -0.4\lambda_0$ , (c)  $\delta\lambda = 0.4t_0$ , and (d)  $\delta\lambda = 0.6\lambda_0$ . A large value of  $\langle S_c(j, j') \rangle$  indicates the existence of quantum synchronization while a small value indicates the lack thereof. In the trivial phase shown in Figs. 5(a) and (b), the synchronization measure is almost uniform with only slight modulations. As there is no synchronization of the mean field amplitudes for random initial conditions [cf. Figs. 3(a) and (b)], this result is not too surprising.

A very different scenario is observed for the boundaries of the chain in the topological phase shown in Figs. 5(c) and (d): While for two oscillators in the bulk,  $\langle S_c(j, j') \rangle$  remains similar to the previous trivial phase, the measure is significantly increased between the two edge oscillators  $j' = 1$  and  $j = 20$  (right bottom corner). Hence, the topological synchronization observed for the mean field amplitudes [cf. Figs. 3(c) and (d)] persists even for the effective quantum model and is therefore not a purely classical effect. Note that the quantity is upper bounded by  $1/4$  due to the Heisenberg uncertainty principle [cf. Eq. (4)]. Furthermore, significant synchronization can be observed for the oscillators  $j' = 1$  and  $j = 3$  as well as  $j' = 18$  and  $j = 20$  resulting from the exponential localization of the edge modes at the boundary of the chain.

Finally, we test the robustness of the edge state synchronization when quantum fluctuations are included. In Fig. 6 we show  $\langle \bar{S}_c(j, j') \rangle$  between the two boundary oscillators ( $j = 1$  and  $j' = 20$ ) in the topological phase with coupling  $\delta\lambda = 0.8\lambda_0$  as a function of the disorder strength  $r$ . Here, the overbar denotes that the quantity is averaged over 100 realizations of disorder. Similar as to the results of the mean field dynamics, also the quantum synchronization of the edges is robust for large amounts of disorder.

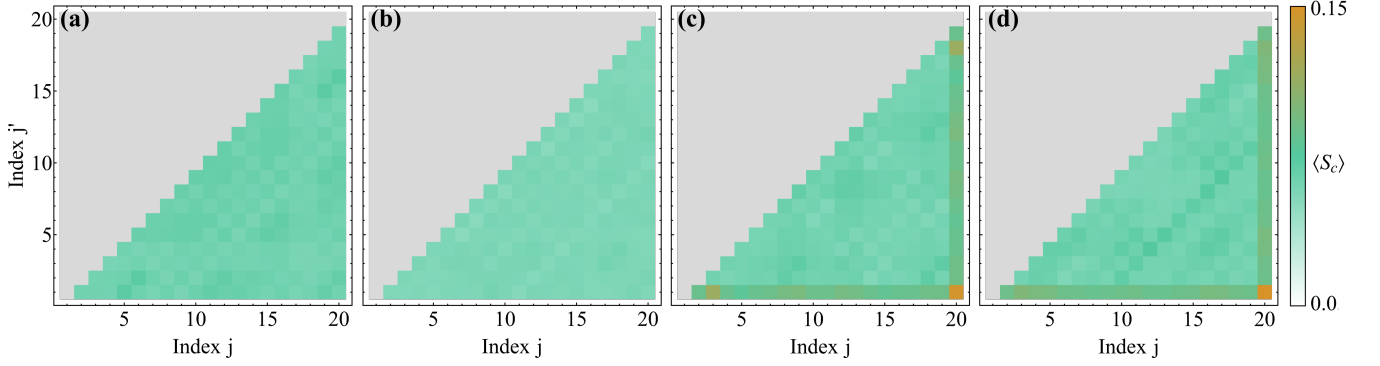


FIG. 5. Time-averaged quantum synchronization measure  $\langle S_c \rangle$  between lattice site  $j$  and  $j'$  of the vdP network corresponding to the mean field dynamics shown in Fig. 3, i.e., with random initial conditions and for different coupling strength (a)  $\delta\lambda = -0.8\lambda_0$ , (b)  $\delta\lambda = -0.4\lambda_0$ , (c)  $\delta\lambda = 0.4\lambda_0$ , and (d)  $\delta\lambda = 0.6\lambda_0$ . While in the trivial phase [panels (a) and (b)] there is no remarkable synchronization between any two lattice sites, in the topological phase the oscillators located at the edges exhibit significantly larger values of synchronization. Parameters:  $\kappa_1 = 5 \cdot 10^{-3}\omega_0$ ,  $\kappa_2 = 2\kappa_1$ ,  $\lambda_0 = 0.25\omega_0$ ,  $\omega_0 t_i = 2 \cdot 10^4$ ,  $\omega_0 t_f = 2.4 \cdot 10^4$ .

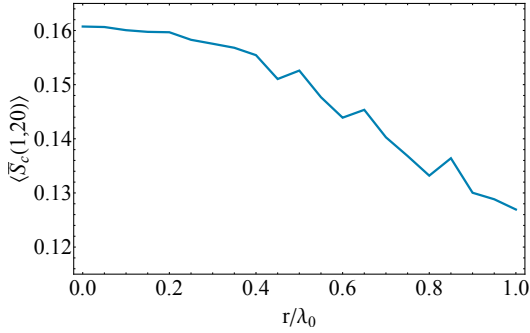


FIG. 6. Quantum synchronization measure  $\langle \bar{S}_c(j, j') \rangle$  between the two edges of  $j = 1$  and  $j' = 20$  in the topological phase ( $\delta\lambda = 0.8\lambda_0$ ) as a function of the disorder strength  $r$ . Disorder is applied to the couplings between neighboring sites via local perturbations uniformly distributed over the interval  $(-r, r)$  and we average over 100 realizations of disorder. The edge state quantum synchronization is topologically protected and robust even for large amounts of disorder. Parameters:  $\kappa_1 = 5 \cdot 10^{-3}\omega_0$ ,  $\kappa_2 = 2\kappa_1$ ,  $\lambda_0 = 0.25\omega_0$ ,  $\omega_0 t_i = 2 \cdot 10^4$ ,  $\omega_0 t_f = 2.4 \cdot 10^4$ .

### C. Example (II): Topological synchronization in the breathing Kagome lattice

#### 1. Edge and corner states in the breathing Kagome lattice

As many fascinating topological effects are inaccessible in one dimension, we also study an example of a two-dimensional systems. We consider here the breathing Kagome lattice [68–71], which is a natural extension of the SSH chain and a paradigmatic model of a so-called higher-order topological insulator (TI) [72]: While an ordinary  $d$ -dimensional TI, such as the SSH chain, exhibits  $d-1$  dimensional topological edge states, in a higher-order

TI  $d-n$  dimensional topological boundary states emerge with  $n > 1$  and the  $d-1$  dimensional edge states are absent. The reason for this peculiar phenomenon is that the boundary of a higher-order TI itself represents an ordinary TI (see Fig. 1). For the breathing Kagome lattice with a generalized chiral, time-reversal and particle-hole symmetry (BDI class), the boundary states are zero-dimensional corner states in the topological phase.

The tight-binding Hamiltonian of the lattice is given by

$$H_{\text{Kag}} = \hbar\lambda_1 \sum_{\langle i,j \rangle \in \Delta} a_i^\dagger a_j + \hbar\lambda_2 \sum_{\langle i,j \rangle \in \nabla} a_i^\dagger a_j, \quad (19)$$

where the two sums are over neighboring sites in the upward and downward triangles, respectively. Throughout we assume  $\lambda_1 \leq 0$  and  $\lambda_2 > 0$  as we are only interested in the transition from trivial ( $\lambda_1/\lambda_2 < -1$ ) to topological insulator phase ( $\lambda_1/\lambda_2 > -1$ ). For  $\lambda_1/\lambda_2 > 0$  there exists another phase transition to a metallic phase at  $\lambda_1/\lambda_2 = 1/2$  [68], however, we do not consider this transition in this work. The related bulk Hamiltonian,

$$\tilde{H}_{\text{Kag}}(k_x, k_y) = \hbar \begin{pmatrix} 0 & h_{12} & h_{13} \\ h_{12}^* & 0 & h_{23} \\ h_{13}^* & h_{23}^* & 0 \end{pmatrix} \quad (20)$$

with  $h_{12} = \lambda_1 + \lambda_2 e^{-ik_x}$ ,  $h_{13} = \lambda_1 + \lambda_2 e^{i(k_x + \sqrt{3}k_y)/2}$  and  $h_{23} = \lambda_1 + \lambda_2 e^{i(k_x - \sqrt{3}k_y)/2}$ , exhibits three bands, one of which is flat [ $\tilde{E}(k_x, k_y)/\hbar = \lambda_1 + \lambda_2$ ]. The band gap closes at the  $\Gamma = (0, 0)$  point for  $\lambda_1 = -\lambda_2$  and a topological phase transition occurs separating the trivial ( $\lambda_1 < -\lambda_2$ ) from the topological ( $\lambda_1 > -\lambda_2$ ) phase. In the latter, zero-energy modes highly localized at the *corners* emerge in the finite lattice. These states are topologically protected

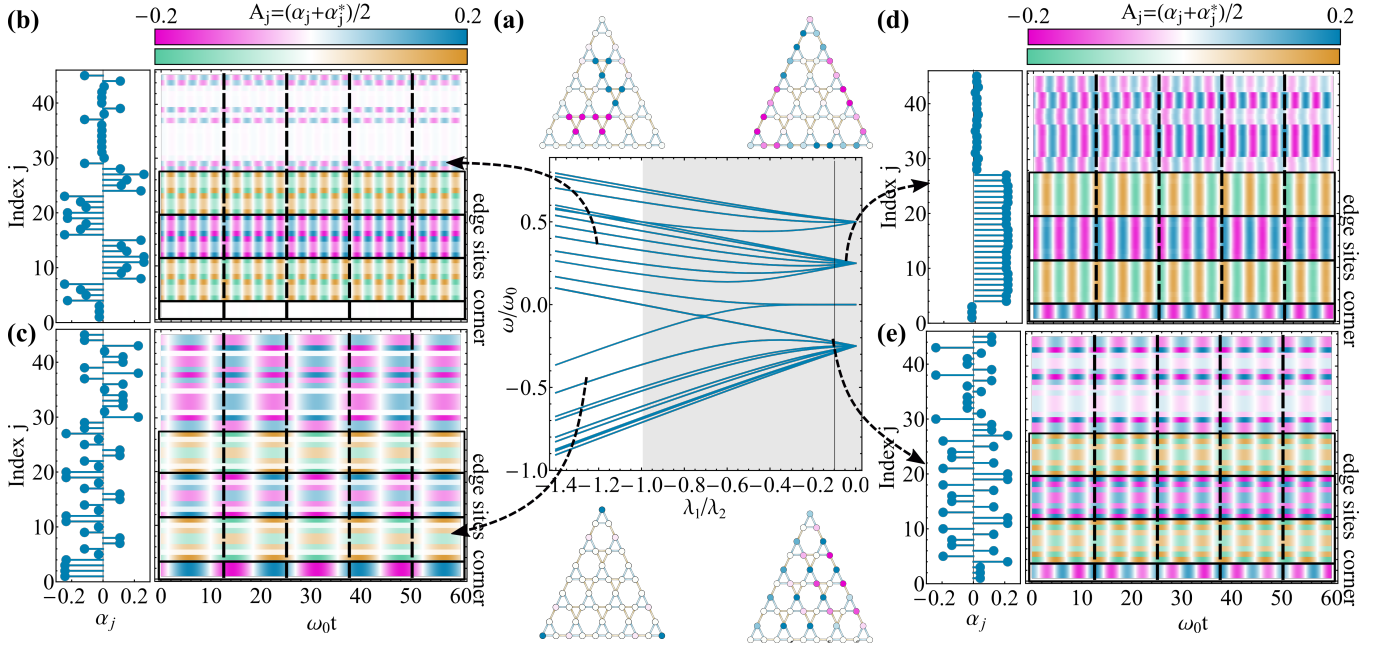


FIG. 7. (a) Eigenspectrum of the breathing Kagome lattice  $\underline{H}_{\text{Kag}}$  as a function of  $\lambda_1$  for 5 upward triangles along each edge, i.e.,  $N = 45$  lattice sites in total. The gray region indicates the nontrivial phase ( $\lambda_1/\lambda_2 > -1.0$ ) of the bulk Hamiltonian. The top and bottom lattices show examples of eigenstates for the three bands and the corner states deep in the topological phase  $\lambda_1/\lambda_2 = -0.1$  as indicated by the vertical line. (b)-(e) Left panels show the amplitude  $a_j^{(l)}$  of the eigenvectors corresponding to the eigenvalues  $\hbar\mu^{(l)}$  marked by the arrows of the eigenspectrum (a), specifically (b)  $\mu^{(l)} = 1.7\lambda_2$  for  $\lambda_1 = -1.2\lambda_2$ , (c)  $\mu^{(l)} = -2.5\lambda_2$  for  $\lambda_1 = -1.3\lambda_2$ , (d)  $\mu^{(l)} = 1.0\lambda_2$  for  $\lambda_1 = -0.05\lambda_2$  (a strict edge state), (e)  $\mu^{(l)} = -1.0\lambda_2$  for  $\lambda_1 = -0.1\lambda_2$ . These eigenstates are the initial states for the dynamics of  $A_j(t)$  of each oscillator  $j$  shown in the right panels. The index  $j$  of lattice sites is chosen in such a way that  $j = 1, 2, 3$  correspond to the corners of the lattice with dynamics shown in pink/blue color scale ( $j = 1$  top corner,  $j = 2$  left corner,  $j = 3$  right corner),  $4 \leq j \leq 11$  to the sites along the left edge with dynamics shown in green/gold color scale,  $12 \leq j \leq 19$  to the sites along the right edge with dynamics shown in pink/blue color scale,  $20 \leq j \leq 27$  to the sites along the bottom edge of the lattice shown in green/gold color scale. The remaining indices ( $28 \leq j \leq 35$ ) with dynamics shown in pink/blue color scale represent bulk oscillators. Parameters:  $\kappa_1 = 5 \cdot 10^{-4}\omega_0$ ,  $\kappa_2 = 10^{-2}\omega_0$ ,  $\lambda_2 = 0.25\omega_0$ .

by an underlying generalized chiral symmetry [73],

$$\begin{aligned} \Gamma_3 \tilde{\underline{H}}_{\text{Kag}} \Gamma_3^{-1} &= \tilde{\underline{H}}_{\text{Kag}}, \\ \Gamma_3 \underline{\tilde{H}}_{\text{Kag}} \Gamma_3^{-1} &= \underline{\tilde{H}}_{\text{Kag}} \\ \tilde{\underline{H}}_{\text{Kag}} + \underline{\tilde{H}}_{\text{Kag}} + \underline{\tilde{H}}_{\text{Kag}} &= 0, \end{aligned} \quad (21)$$

where the chiral operator  $\Gamma_3$  has eigenvalues 1,  $\exp(i2\pi/3)$ , and  $\exp(-i2\pi/3)$ . Note the different overscripts in Eq. (21).

In Fig. 7(a) we show the energy spectrum of the breathing Kagome lattice containing 15 upward triangles as a function of  $\lambda_1$ , i.e. the coupling within upward triangles. Above and below the spectrum, exemplary eigenstates of the different bands and the band gap are shown for the parameter  $\lambda_1/\lambda_2 = -0.1$ : The top band contains only strict bulk states which have (almost) no overlap with the boundary of the lattice as shown in the top left. The bottom band on the other hand contains states delocalized over the lattice as shown in the bottom right lattice. In contrast, the middle band contains edge states which are localized at the boundary of the lattice as shown in

the top right figure. Lastly, the band gap located at zero energy consists of three degenerate states exponentially localized at the corners of the lattice, see the left bottom lattice. The latter are topologically protected by the generalized chiral symmetry.

## 2. Topological effects on synchronization at the mean field level

In the following we investigate the mean field dynamics of the vdP network in the breathing Kagome lattice. To this end, the matrix governing the system dynamics without dissipation in Eq. (8) is given by

$$\underline{\underline{H}} = \hbar\omega_0 \underline{1} + \underline{H}_{\text{Kag}}, \quad (22)$$

where  $\underline{H}_{\text{Kag}}$  denotes the matrix corresponding to the Hamiltonian defined in Eq. (19).

Following our analytic considerations of Sec. II C and the results of the previous Sec. III B 2, we expect that the oscillatory dynamics is dominated by the closed system

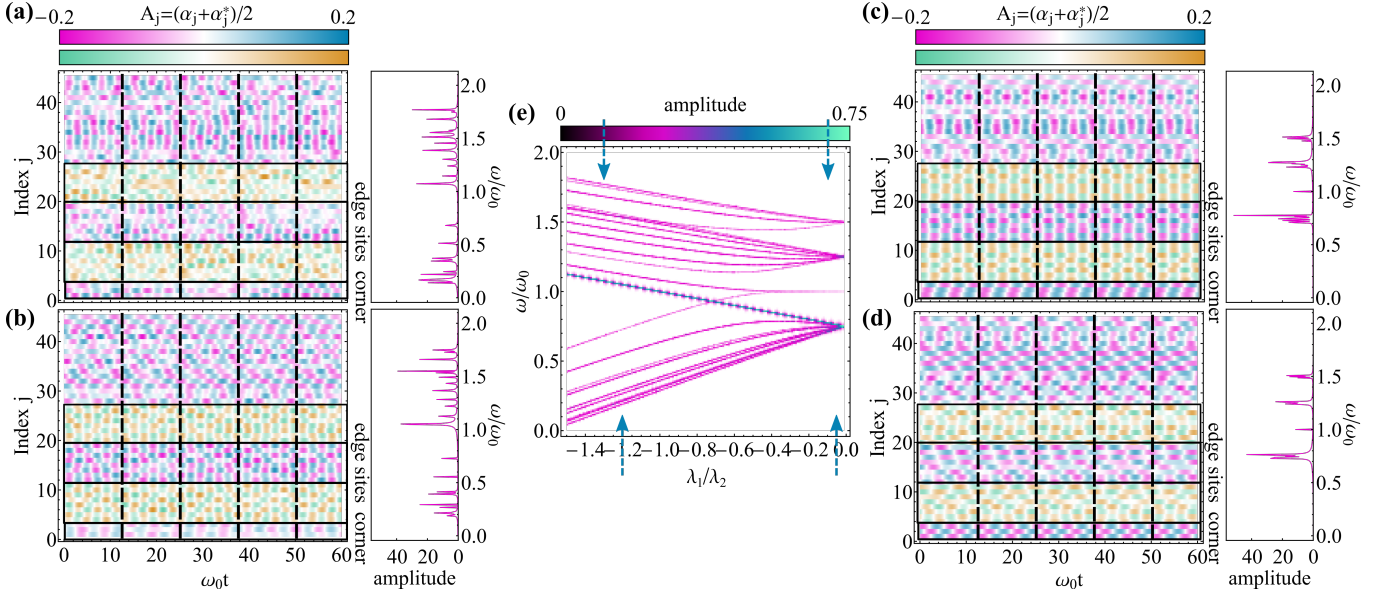


FIG. 8. (a)–(d) Left panels show the amplitude dynamics  $A_j(t)$  of oscillator  $j$  – where we choose an ordering according to Fig. 7 and two color scales to differentiate corner, different edge and bulk lattice sites – in the vdP Kagome network with random initial conditions for different couplings: (a)  $\lambda_1/\lambda_2 = -1.3$ , (b)  $\lambda_1/\lambda_2 = -1.2$ , (c)  $\lambda_1/\lambda_2 = -0.1$ , and (d)  $\lambda_1/\lambda_2 = -0.05$  [also marked by the blue arrows in panel (e)]. The right panels show the frequency spectrum of the dynamics shown in the left panels obtained via discrete Fourier analysis. (e) Frequency spectrum obtained from the oscillator dynamics for random initial conditions as function of the upward-triangle coupling  $\lambda_1$ , where for each coupling 10 realizations of initial conditions are averaged. Parameters:  $\kappa_1 = 5 \cdot 10^{-4} \omega_0$ ,  $\kappa_2 = 10^{-2} \omega_0$ ,  $\lambda_2 = 0.25 \omega_0$ .

dynamics given by Hamiltonian (22). In Figs. 7(b)–(e) we show the amplitude  $A_j(t)$  of each oscillator  $j$  as a function of time with eigenstates  $\alpha^{(l)}$  as initial states; shown in the left panels of Figs. 7(b)–(e). We start our discussion in the trivial phase shown in Figs. 7(b) and (c), where the total vdP network is synchronized, oscillating with frequency  $\omega_0 + \mu^{(l)}$  [a larger frequency in panel (b) where  $\mu^{(l)} > 0$  and a smaller frequency in panel (c) where  $\mu^{(l)} < 0$ ] and oscillation amplitudes proportional to the chosen initial eigenstate  $\alpha^{(l)}$ . As in the previous example (I) the dynamics in the trivial phase is thus given by  $\alpha(t) = c\alpha^{(l)} \exp\{-i[\omega + \mu^{(l)}]t\}$ .

In Figs. 7(d) and (e) we show examples of the dynamics in the topological phase. If the initial eigenstate is completely delocalized across the lattice [cf. Fig. 7(e)], the oscillator dynamics follows the same principles as discussed in Sec. III B 2, i.e. complete synchronized oscillations with common frequency  $\omega_0 + \mu^{(l)}$  except of the three corners (index  $j = 1, 2, 3$ ), which amplitudes oscillate with the intrinsic frequency  $\omega_0$ . The latter additionally exhibit a temporal amplitude modulation as a result of the finite amplitude of the initial state at the corners, i.e.  $A_j(t) = \bar{A}_j \cos\{[\omega_0 + \mu^{(l)}]t\} + \bar{A}_{\text{corner}} \cos(\omega_0 t)$ , where  $\bar{A}_j$  and  $\bar{A}_{\text{corner}}$  reflect the mixture of the two participating frequencies.

However, if the initial eigenstate is localized at the edges as shown in Fig. 7(d) we additionally observed excitation of all bulk lattice oscillating with a common fre-

quency. However, their frequency does not match the corner nor the edge oscillators. Moreover, their amplitude is not constant but exhibits modulations over time. The reason for this effect is that the top band in Fig. 7(a) consists of strict bulk states without participation of any edge or corner lattice sites. Due to the nonlinearity in the dynamics, these strict bulk states may grow, yet, as a superposition of many of those, which may explain the amplitude modulations.

We are now interested whether the topological synchronization with random initial conditions also carries over to the two dimensional model. In Figs. 8(a)–(d) we show in the left panels the oscillator dynamics  $A_j(t)$  as function of time for different coupling strengths with ordering of the oscillators according to Fig. 7. In the corresponding right panels we show the frequency spectrum of the particular realization of oscillator dynamics obtained via discrete Fourier transformation. In the trivial phase shown in Figs. 8(a) and (b) clear signatures of synchronization are again missing and the dynamics is governed by a randomly distributed superposition of many eigenstates oscillating with different frequencies. The emergent complex oscillation pattern may exhibit temporal synchronized structures, however, these vanish again over longer times.

By contrast in the topological phase, shown in Figs. 8(c) and (d), the dynamics of the network appears more structured and synchronized. The reason for this is that fewer frequencies are available in the eigenspec-

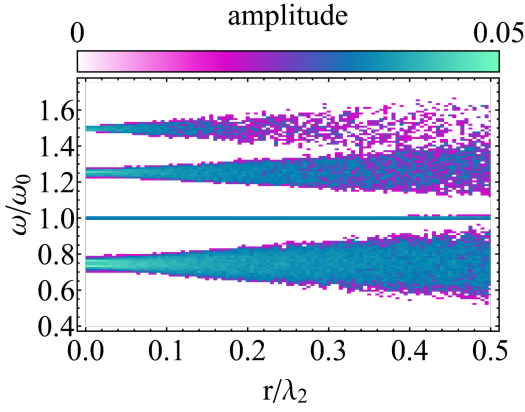


FIG. 9. Frequency spectrum of the vdP network for  $\lambda_1 = -0.05\lambda_2$  obtained via discrete Fourier transformation as a function of the disorder strength  $r$ . Disorder is applied to the couplings between neighboring sites via local perturbations uniformly distributed over the interval  $(-r, r)$ . While the band frequencies are strongly affected by the disorder, the corner modes located at  $\omega = \omega_0$  are robust, even for large amounts of disorder. Parameters:  $\kappa_1 = 5 \cdot 10^{-4}\omega_0$ ,  $\kappa_2 = 10^{-2}\omega_0$ ,  $\lambda_2 = 0.25\omega_0$ , 10 realizations of random initial states for each data value of  $r$ .

trum of  $\underline{H}_{\text{Kag}}$ , and especially in the specific realization that there exists a dominant frequency as indicated by the large peak in the frequency spectra (see right panels). However, most notably the oscillators located at the three corners of the lattice ( $j = 1, 2, 3$ ) are phase locked (cf. Sec. II A) and oscillate with the intrinsic frequency  $\omega_0$ . Thus, as in the SSH chain, the topological character of the lattice is reflected in the amplitude oscillations even for random initial conditions. This also allows us to reconstruct the full eigenspectrum of the topological coupling matrix  $\underline{H}_{\text{Kag}}$  via discrete Fourier analysis of oscillator dynamics, which we show in Fig. 8(e) averaged over 10 realizations of initial conditions. The reconstruction of the frequency spectrum also reveals the existence of a highly degenerate eigenvalue spanning diagonally across with a much larger amplitude (blue) than the other eigenvalues (pink).

Lastly, we test the robustness of the observed corner state synchronization. As the corner states of the breathing Kagome lattice are topologically protected by a generalized chiral symmetry (cf. Sec. III C 1), we expect protection of the corner state synchronization. In Fig. 9 we show the frequency spectrum of the discrete Fourier analysis for the coupling  $\lambda_1 = -0.05\lambda_2$  as a function of the disorder strength  $r$  for 10 realizations. The topological zero-energy corner modes are robust against disorder strengths as large as  $r = 0.4\lambda_2$  before they are affected by the perturbations. In contrary, the bands spread over a wider range as the disorder strength is increased. Furthermore, this analysis also shows that the edge states are *not* topologically protected in the higher order TI.

### 3. Quantum signatures of topological synchronization

After we have observed in the previous section that topological protected synchronization of the mean field amplitudes also exists for a higher-order TI, we now analyze its quantum fluctuations quantified in terms of  $\langle S_c(j, j') \rangle$  [cf. Eq. (5)] between two lattice sites  $j$  and  $j'$ . Similar as to case of the SSH model we choose the mean field amplitudes after relaxation as initial conditions and focus on the case of random initial conditions corresponding to the dynamics shown in Figs. 8(a)–(d).

In Figs. 10(a)–(d) we show the time-averaged quantum synchronization measure  $\langle S_c(j, j') \rangle$  for different couplings strengths (a)  $\lambda_1/\lambda_2 = -1.3$ , (b)  $\lambda_1/\lambda_2 = -1.2$ , (c)  $\lambda_1/\lambda_2 = -0.1$ , and (d)  $\lambda_1/\lambda_2 = -0.05$ . The ordering of the lattice sites corresponds to Fig. 9, especially  $j', j = 1, 2, 3$  are the corners of the lattice. We are mostly interested in the latter as they are expected to show quantum signatures of synchronization. In accordance with the classical mean field amplitudes of Figs. 8(a) and (b), the synchronization measure is almost uniform in the trivial phase shown in Figs. 10(a) and (b).

However, in the topological phase shown in Figs. 10(c) and (d) we observe that the oscillators located the corners ( $j', j = 1, 2, 3$ ) are significantly synchronized with one another as indicated by the large value of  $\langle S_c(j, j') \rangle$  at the left bottom corner (highlighted by the pink dashed circle). As a reminder the quantity is bounded by  $1/4$  [cf. Eq. (4)]. Moreover, the quantum synchronization measure indicates that all three corner oscillators are synchronized with the edges and parts of the bulk. This feature is also present for the two edges of the SSH model [cf. III B 3]. By contrast, for any two bulk oscillators,  $\langle S_c(j, j') \rangle$  remains similar to the previous trivial phase.

Finally, we test the topological protection of the corner state synchronization at the quantum level. In Fig. 11 we show  $\langle \bar{S}_c(j, j') \rangle$  between the corners [ $(j = 1, j' = 2)$ ,  $(j = 1, j' = 3)$  and  $(j = 2, j' = 3)$ ] in the topological phase ( $\delta\lambda = 0.8\lambda_0$ ) as a function of the disorder strength  $r$ . Here, the overbar denotes the average over 100 realizations of disorder. Consistent with the previous observations, also the quantum synchronization of the corners is robust for large amounts of disorder.

## IV. DISCUSSION

An adequate formulation of topological insulators can be provided within the framework of solid state band theory and it is thus far from obvious whether and how their effects persist if affected by dissipation. Moreover, in the case investigated in this work dissipation represents a necessary resource to drive the system far away from equilibrium. Remarkably, despite the tremendous consequences open system conditions in combination with nonlinearities can have on the system dynamics, our examples show that topological features remain in such a scenario, which allows us to utilize them in our favor.

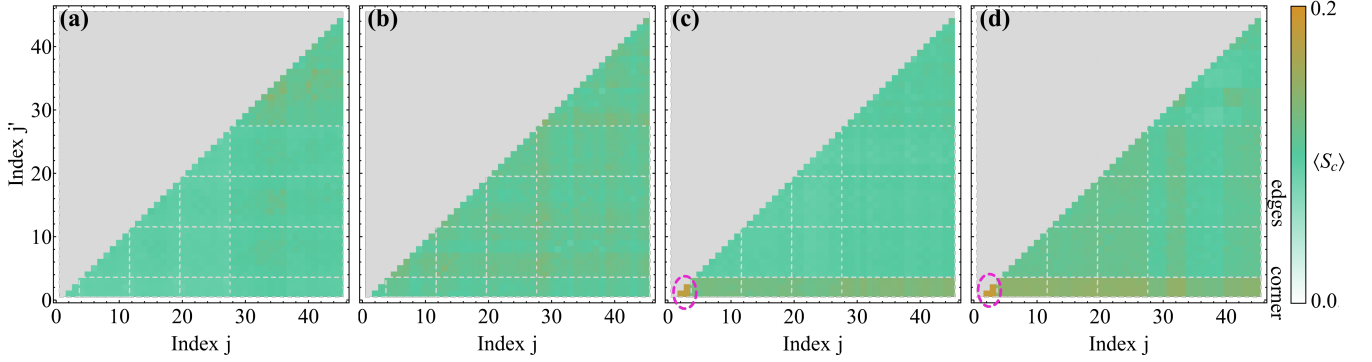


FIG. 10. Time-averaged quantum complete synchronization measure  $\langle S_c \rangle$  between lattice site  $j$  and  $j'$  of the vdP Kagome network corresponding to the mean field dynamics shown in Fig. 9, i.e., with random initial conditions and for different coupling strength (a)  $\lambda_1/\lambda_2 = -1.3$ , (b)  $\lambda_1/\lambda_2 = -1.2$ , (c)  $\lambda_1/\lambda_2 = -0.1$ , and (d)  $\lambda_1/\lambda_2 = -0.05$ . The ordering of the lattice sites is the same as in Fig. 9 especially  $j = 1, 2, 3$  correspond to the corners of the lattice. While in the trivial phase [panels (a) and (b)] there is no clear pattern of synchronization between any two lattice sites, in the topological phase the oscillators located at the corners (encircled in pink) exhibit significantly larger values of synchronization. Parameters:  $\kappa_1 = 5 \cdot 10^{-4} \omega_0$ ,  $\kappa_2 = 10^{-2} \omega_0$ ,  $\lambda_2 = 0.25 \omega_0$ ,  $\omega_0 t_i = 2 \cdot 10^4$ ,  $\omega_0 t_f = 2.3 \cdot 10^4$ .

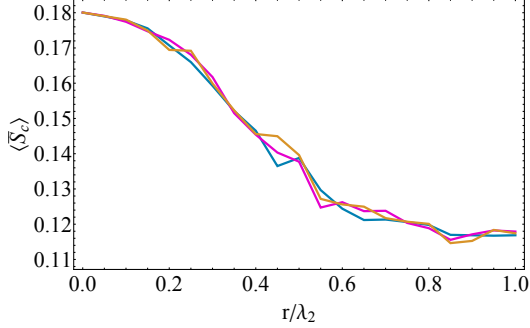


FIG. 11. Quantum synchronization measure  $\langle \bar{S}_c(j, j') \rangle$  between the three corners [ $(j = 1, j' = 2)$ ,  $(j = 1, j' = 3)$  and  $(j = 2, j' = 3)$ ] in the topological phase ( $\lambda_1/\lambda_2 = -0.05$ ) as a function of the disorder strength  $r$ . Disorder is applied to the couplings between neighboring sites via local perturbations uniformly distributed over the interval  $(-r, r)$  and we average over 100 realizations of disorder. The corner state quantum synchronization is topologically protected and robust even for large amounts of disorder. Parameters:  $\kappa_1 = 5 \cdot 10^{-4} \omega_0$ ,  $\kappa_2 = 10^{-2} \omega_0$ ,  $\lambda_2 = 0.25 \omega_0$ ,  $\omega_0 t_i = 2 \cdot 10^4$ ,  $\omega_0 t_f = 2.3 \cdot 10^4$ .

The observed topological boundary synchronization at the mean field level is not restricted to the two specific examples investigated in this work, but also applies to other topological insulator lattices as long as zero-energy modes are present. The reason for this is that the edge modes  $\alpha_{\text{edge}}$  with zero energy are always a solution to the differential equation  $\dot{\alpha} = -(i/\hbar) \underline{H}_{\text{top}} \alpha$ , i.e.,  $\alpha_{\text{edge}}$  is an element of the kernel of  $\underline{H}_{\text{top}}$ . Hence, any small perturbation, which is provided due to the coupling to neighboring lattice sites, will excite these modes. Consequently, they will oscillate synchronized with the intrinsic frequency  $\omega_0$ . Moreover, they inherit the topological protection

known from closed systems with remarkable robust dynamics against local (symmetry-preserving) disorder and even random initial conditions.

Often when fluctuations are considered synchronization is lost. Our results, however, show signatures of boundary synchronization beyond the classical mean field approximation. Furthermore, it remains unaffected for large amounts of local disorder in the couplings due to the underlying topology, which has the advantage that even if perfect fabrication of the lattice is impossible our findings can still be observed. This makes our results appealing for experimental realizations, two of which we discuss in more detail in the next section.

Lastly, let us highlight the ability to reconstruct the full eigenspectrum of the underlying topological lattice from the oscillator (mean field) dynamics alone. In our numerical studies with only 10 realizations the full spectra of the (closed) SSH and Kagome lattice could already be obtained. This holds the potential of a new experimental mechanism to measure eigenspectra of a topological systems from the dynamics of a nonlinear system far away from equilibrium and without preparation of an initial state.

## V. EXPERIMENTAL PROPOSAL

There are many possible experimental platforms where topological synchronization may be observed in the mean field (classical) as well as the quantum regime. To realize the dynamics of a single vdP oscillator in a quantum system two different implementations have been suggested: The first one uses trapped ions [8, 46] as an experimental platform while the second one focuses on optomechanics [46, 47]. Both of these proposals bear the potential of vdP oscillator networks and thus to observe the previ-

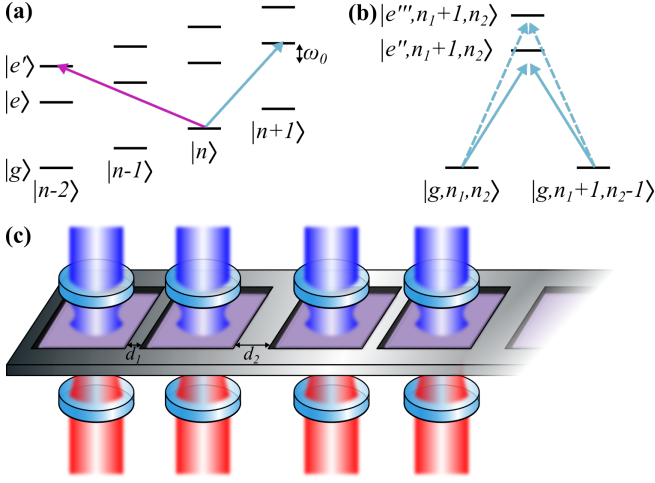


FIG. 12. Potential experimental realizations of topologically coupled van der Pol oscillators. (a) and (b) Trapped ions implementation: (a) Level scheme for an ion with trap frequency  $\omega_0$ . By exciting the blue sideband of the transition  $|g\rangle \rightarrow |e\rangle$  negative damping may be realized (blue arrow). Simultaneously driving the double red sideband transition  $|g\rangle \rightarrow |e'\rangle$  allows one to realize the nonlinear damping (pink arrow). (b) Two modes may be coupled via off-resonant excitation of blue sidebands of  $|g\rangle \rightarrow |e''\rangle$  or  $|g\rangle \rightarrow |e'''\rangle$ , which realizes the alternating couplings between nearest neighbors. (c) Optomechanical implementation: The so-called ‘membrane in the middle’-setup allows to realize a van der pol oscillator with nonlinear damping via a laser detuned to the red two-phonon sideband and negative damping by a laser on the blue one-phonon sideband. Mechanical coupling with alternating distances then allows to implement the topological lattice interactions.

ously discussed topological synchronization phenomena. Therefore, we summarize both of them and discuss their extensions towards topological lattices.

A motional mode of a trapped ion in the Lamb-Dicke regime and when the trapping potentials are tight with ground state  $|g\rangle$  and excited state  $|e\rangle$  is represented as an harmonic oscillator with frequency  $\omega_0$ . In order to fulfill the required conditions, i.e., negative and nonlinear damping, two side bands are excited simultaneously [74]: The first laser drives the transition  $|g\rangle \rightarrow |e\rangle$  but blue detuned by  $\omega_0$  which absorbs one phonon after subsequent decay to the ground state [see Fig. 12(a)]. The second laser is double red detuned by  $-2\omega_0$  and excites to a state  $|e'\rangle$  such that after relaxation to the ground state two phonons have been emitted. The combination of these two processes approximately implement the dissipators of each oscillator in Eq. (7). Specific parameters for an implementation with  $^{171}\text{Yb}^+$  are provided in Ref. [8] and references therein.

Additionally, the bosonic modes of neighboring trapped ions need to be coupled: By off-resonantly exciting an additional level  $|e''\rangle$  via a blue sideband [see Fig. 12(b)] an effective Hamiltonian  $H = \hbar\lambda_1(a_j^\dagger a_{j+1} +$

$a_{j+1}^\dagger a_j)$  for the phonon exchange between oscillator  $j$  and  $j+1$  may be implemented. Using the same strategy but with an additional level  $|e'''\rangle$  leads to a different coupling strength  $\lambda_2$ . In this way the alternating interactions necessary for topological effects to emerge may be realized in trapped ion experiments.

Another experimental setup where our proposal could be implemented is provided by optomechanics as sketched in Fig. 12(c): The so-called ‘membrane-in-the-middle’-setup [75–78] allows to realize two-phonon processes [79] as the cavity mode is parametrically modulated by the *squared* position of a movable membrane. The Hamiltonian of a single mechanical membrane inside a cavity driven on the red two-phonon resonance (in the good-cavity limit and focusing on the resonant terms) is given by  $H_{\text{opt}} = \hbar g(a^\dagger a^\dagger b + \text{h.c.})$  [79]. The dynamics of the coupled system is described by the master equation

$$\dot{\rho} = -\frac{i}{\hbar} [H_{\text{opt}}, \rho] + \gamma_c \mathcal{D}[b] \rho + \gamma(1 + \bar{n}) \mathcal{D}[a] \rho + \gamma \bar{n} \mathcal{D}[a^\dagger] \rho, \quad (23)$$

where  $\bar{n}$  is the thermal phonon number. The Heisenberg equation of motion for the cavity is  $\dot{b} = -iga - \gamma_c b/2$ . Adiabatically eliminating the optical mode and defining  $\kappa_2 \equiv g^4/\gamma_c$  results in the two-phonon dissipator of Eq. (7). However, the other two linear dissipators in Eq. (23) are related via the thermal phonon occupation  $\bar{n}$ , such that one-phonon gain cannot be larger than the one-phonon loss. Therefore, another laser driving the cavity on the blue one-phonon sideband is needed [46, 47]. Nevertheless, compared to Eq. (7) an additional one-phonon loss term  $\gamma(1 + \bar{n}) \mathcal{D}[a] \rho$  is present. If we assume  $\gamma(1 + \bar{n}) \ll \kappa_1$ , the influence of this additional term can be completely neglected at the mean field level as it only results in an effective damping rate  $\tilde{\kappa}_1 = \kappa_1 - \gamma(1 + \bar{n})$ . Also our results in the quantum regime remain unchanged if one would include such a linear loss channel (see App. D).

When two membranes share a common support they are mechanically coupled expressed via the Hamiltonian  $H = \tilde{\lambda}_j x_j x_{j+1}$  where  $x_j = \sqrt{\hbar/2m\omega_0}(a_j^\dagger + a_j)$  with oscillator mass  $m$ . After the rotating-wave approximation and with the definition  $\lambda_j = 2m\omega_0 \tilde{\lambda}_j$ , the Hamiltonian becomes equivalent to the coupling Hamiltonian (6). The interaction strengths between two oscillators may be modified by altering the distance between neighboring membranes; see Fig. 12(c) for an example of the SSH model with staggered distances  $d_1$  and  $d_2$ . Thus, also optomechanics has the potential to observe topologically protected synchronization in a network of quantum vdP oscillators.

## VI. CONCLUSIONS

We investigate the interplay of topology and synchronization in a network of coupled quantum van der Pol oscillators simulating different topological insulator lattices. We show via a linear stability analysis that the

dynamics of the resulting topological lattice of oscillators at the mean field level is governed by the eigenvalues of the topological Hamiltonian and thus reflects the features of the underlying topology even though the system is highly nonlinear and far away from equilibrium. Furthermore, we derive an effective quantum model which takes quadratic quantum fluctuations about the classical trajectories into account in order to investigate quantum signatures of topological synchronization beyond the mean field approximation. For two specific examples of topological insulator models in one and two dimensions we demonstrate that in the nontrivial phase, synchronization at the boundaries is always present independent of initial conditions, and that it inherits the protection against perturbations from the underlying lattice structure. In terms of a Fourier analysis of the oscillations, we are able to reconstruct the full topological eigenspectrum of the system, which not only represents a possible route to observe topological synchronization of boundary modes experimentally, e.g. in trapped ions or optomechanics, but an additional opportunity to measure topological eigenspectra solely from the dynamics of a highly nonlinear and open system.

Researchers and engineers make great efforts to fabricate dynamical systems which are nearly identical in order to facilitate the emergence of synchronized collective behavior in large networks. However, our work demonstrates a general advantage of topologically motivated interactions in the design of potential experiments and devices as fabrication errors and longterm degradation are circumvented in this way. This is especially important in networks where specific nodes need special protection. While the examples investigated in this work possess zero dimensional protected boundary states, our

work can easily be extended to host higher dimensional topologically protected states for additional robust network nodes. Synchronization is desirable in situations where high oscillating power, strong coherence, or low phase noise are needed, such as lasers [80], phase-locked loops [81], Josephson junction arrays [82, 83], spin-torque resonators [84], quantum heat engines [85] or power grids [86]. Even today, the originally observed phenomenon of clock synchronization remains a crucial application for modern communication networks [87–89] and has recently been extended to quantum networks and quantum key distribution protocols [89–91]. All of these examples require the synchronized behavior to be robust to fulfill their desired purpose and will benefit from the application of topology. Given the universality of the concept of combining nonlinear dynamics in open quantum systems with topological phases of matter, we expect that our approach could be successfully applied also to other systems where robust dynamics is crucial.

#### ACKNOWLEDGMENTS

We thank M. T. Eiles and W. Munro for invigorating discussions and for insightful comments on the manuscript. C.W.W. acknowledges support from the Max-Planck Gesellschaft via the MPI-PKS Next Step fellowship and is financially supported by the Deutsche Forschungsgemeinschaft (DFG, German Research Foundation) – Project No. 496502542 (WA 5170/1-1). G.P. acknowledges support from the Spanish Ministry of Science and Innovation through the grant No. PID2020-117787GB-I00 and from the CSIC Research Platform on Quantum Technologies PTI-001.

- 
- [1] A. Pikovsky, J. Kurths, M. Rosenblum, and J. Kurths, *Synchronization: a universal concept in nonlinear sciences* (Cambridge university press, Cambridge University Press, 2003).
  - [2] S. H. Strogatz, *Nonlinear dynamics and chaos: with applications to physics, biology, chemistry, and engineering* (CRC Press, 2018).
  - [3] A. Jenkins, Self-oscillation, *Phys. Rep.* **525**, 167 (2013).
  - [4] C. W. Wächter, P. Strasberg, S. H. L. Klapp, G. Schaller, and C. Jarzynski, Stochastic thermodynamics of self-oscillations: the electron shuttle, *New J. Phys.* **21**, 07300921 (2019).
  - [5] C. W. Wächter, P. Strasberg, and G. Schaller, Proposal of a realistic stochastic rotor engine based on electron shuttling, *Phys. Rev. Applied* **12**, 024001 (2019).
  - [6] P. Strasberg, C. W. Wächter, and G. Schaller, Autonomous implementation of thermodynamic cycles at the nanoscale, *Phys. Rev. Lett.* **126**, 180605 (2021).
  - [7] O. Zhirov and D. L. Shepelyansky, Quantum synchronization, *Eur. Phys. J. D* **38**, 375 (2006).
  - [8] T. E. Lee and H. R. Sadeghpour, Quantum synchronization of quantum van der pol oscillators with trapped ions, *Phys. Rev. Lett.* **111**, 234101 (2013).
  - [9] T. E. Lee, C.-K. Chan, and S. Wang, Entanglement tongue and quantum synchronization of disordered oscillators, *Phys. Rev. E* **89**, 022913 (2014).
  - [10] M. Xu, D. A. Tieri, E. C. Fine, J. K. Thompson, and M. J. Holland, Synchronization of two ensembles of atoms, *Phys. Rev. Lett.* **113**, 154101 (2014).
  - [11] A. Roulet and C. Bruder, Quantum synchronization and entanglement generation, *Phys. Rev. Lett.* **121**, 063601 (2018).
  - [12] N. Lörch, E. Amitai, A. Nunnenkamp, and C. Bruder, Genuine quantum signatures in synchronization of anharmonic self-oscillators, *Phys. Rev. Lett.* **117**, 073601 (2016).
  - [13] N. Lörch, S. E. Nigg, A. Nunnenkamp, R. P. Tiwari, and C. Bruder, Quantum synchronization blockade: Energy quantization hinders synchronization of identical oscillators, *Phys. Rev. Lett.* **118**, 243602 (2017).
  - [14] S. Sonar, M. Hajdušek, M. Mukherjee, R. Fazio, V. Vedral, S. Vinjanampathy, and L.-C. Kwek, Squeezing enhances quantum synchronization, *Phys. Rev. Lett.* **120**, 163601 (2018).

- [15] A. Roulet and C. Bruder, Synchronizing the smallest possible system, *Phys. Rev. Lett.* **121**, 053601 (2018).
- [16] G. Karpat, I. Yalçinkaya, and B. Çakmak, Quantum synchronization of few-body systems under collective dissipation, *Phys. Rev. A* **101**, 042121 (2020).
- [17] N. Es'haqi Sani, G. Manzano, R. Zambrini, and R. Fazio, Synchronization along quantum trajectories, *Phys. Rev. Research* **2**, 023101 (2020).
- [18] M. Koppenhöfer, C. Bruder, and A. Roulet, Quantum synchronization on the ibm q system, *Phys. Rev. Research* **2**, 023026 (2020).
- [19] D. J. Thouless, M. Kohmoto, M. P. Nightingale, and M. den Nijs, Quantized hall conductance in a two-dimensional periodic potential, *Phys. Rev. Lett.* **49**, 405 (1982).
- [20] F. D. M. Haldane, Model for a quantum hall effect without landau levels: Condensed-matter realization of the "parity anomaly", *Phys. Rev. Lett.* **61**, 2015 (1988).
- [21] X.-G. Wen, Colloquium: Zoo of quantum-topological phases of matter, *Rev. Mod. Phys.* **89**, 041004 (2017).
- [22] J. E. Moore, Topological insulators: The next generation, *Nat. Phys.* **5**, 378 (2009).
- [23] J. E. Moore, The birth of topological insulators, *Nature* **464**, 194 (2010).
- [24] M. Z. Hasan and C. L. Kane, Colloquium: topological insulators, *Rev. Mod. Phys.* **82**, 3045 (2010).
- [25] M. Z. Hasan and J. E. Moore, Three-dimensional topological insulators, *Annu. Rev. Condens. Matter Phys.* **2**, 55 (2011).
- [26] S. Mittal, J. Fan, S. Faez, A. Migdall, J. Taylor, and M. Hafezi, Topologically robust transport of photons in a synthetic gauge field, *Phys. Rev. Lett.* **113**, 087403 (2014).
- [27] S. Diehl, E. Rico, M. A. Baranov, and P. Zoller, Topology by dissipation in atomic quantum wires, *Nat. Phys.* **7**, 971 (2011).
- [28] C.-E. Bardyn, M. A. Baranov, C. V. Kraus, E. Rico, A. Imamoglu, P. Zoller, and S. Diehl, Topology by dissipation, *New J. Phys.* **15**, 085001 (2013).
- [29] Z. Gong, Y. Ashida, K. Kawabata, K. Takasan, S. Higashikawa, and M. Ueda, Topological phases of non-hermitian systems, *Phys. Rev. X* **8**, 031079 (2018).
- [30] F. K. Kunst, E. Edvardsson, J. C. Budich, and E. J. Bergholtz, Biorthogonal bulk-boundary correspondence in non-hermitian systems, *Phys. Rev. Lett.* **121**, 026808 (2018).
- [31] S. Yao and Z. Wang, Edge states and topological invariants of non-hermitian systems, *Phys. Rev. Lett.* **121**, 086803 (2018).
- [32] K. Kawabata, K. Shiozaki, M. Ueda, and M. Sato, Symmetry and topology in non-hermitian physics, *Phys. Rev. X* **9**, 041015 (2019).
- [33] F. Song, S. Yao, and Z. Wang, Non-hermitian skin effect and chiral damping in open quantum systems, *Phys. Rev. Lett.* **123**, 170401 (2019).
- [34] C.-H. Liu, K. Zhang, Z. Yang, and S. Chen, Helical damping and dynamical critical skin effect in open quantum systems, *Phys. Rev. Research* **2**, 043167 (2020).
- [35] A. McDonald, R. Hanai, and A. A. Clerk, Nonequilibrium stationary states of quantum non-hermitian lattice models, *Phys. Rev. B* **105**, 064302 (2022).
- [36] D. Smirnova, D. Leykam, Y. Chong, and Y. Kivshar, Nonlinear topological photonics, *Appl. Phys. Rev.* **7**, 021306 (2020).
- [37] D. D. Solnyshkov, O. Bleu, B. Teklu, and G. Malpuech, Chirality of topological gap solitons in bosonic dimer chains, *Phys. Rev. Lett.* **118**, 023901 (2017).
- [38] G. Harari, M. A. Bandres, Y. Lumer, M. C. Rechtsman, Y. D. Chong, M. Khajavikhan, D. N. Christodoulides, and M. Segev, Topological insulator laser: theory, *Science* **359**, 4003 (2018).
- [39] M. A. Bandres, S. Wittek, G. Harari, M. Parto, J. Ren, M. Segev, D. N. Christodoulides, and M. Khajavikhan, Topological insulator laser: Experiments, *Science* **359**, 4005 (2018).
- [40] R. Chaunsali and G. Theocharis, Self-induced topological transition in phononic crystals by nonlinearity management, *Phys. Rev. B* **100**, 014302 (2019).
- [41] Y. Wang, L.-J. Lang, C. H. Lee, B. Zhang, and Y. Chong, Topologically enhanced harmonic generation in a nonlinear transmission line metamaterial, *Nat. Commun.* **10**, 1 (2019).
- [42] C. Wächter, V. Bastidas, G. Schaller, and W. Munro, Dissipative nonequilibrium synchronization of topological edge states via self-oscillation, *Phys. Rev. B* **102** (2020).
- [43] T. Kotwal, F. Moseley, A. Stegmaier, S. Imhof, H. Brand, T. Kießling, R. Thomale, H. Ronellenfitsch, and J. Dunkel, Active topoelectrical circuits, *Proc. Natl. Acad. Sci. U.S.A.* **118**, e2106411118 (2021).
- [44] K. Sone, Y. Ashida, and T. Sagawa, Topological synchronization of coupled nonlinear oscillators, *Phys. Rev. Research* **4**, 023211 (2022).
- [45] B. Van der Pol, theory of the amplitude of free forced triode vibrations, *Radio Rev.* **1**, 701 (1920).
- [46] S. Walter, A. Nunnenkamp, and C. Bruder, Quantum synchronization of a driven self-sustained oscillator, *Phys. Rev. Lett.* **112**, 094102 (2014).
- [47] S. Walter, A. Nunnenkamp, and C. Bruder, Quantum synchronization of two van der pol oscillators, *Ann. Phys.* **527**, 131 (2015).
- [48] V. M. Bastidas, I. Omelchenko, A. Zakharova, E. Schöll, and T. Brandes, Quantum signatures of chimera states, *Phys. Rev. E* **92**, 062924 (2015).
- [49] H. P. Breuer and F. Petruccione, *The Theory of Open Quantum Systems* (Oxford University Press, Oxford, 2002).
- [50] G. Schaller, *Open Quantum Systems Far from Equilibrium* (Lect. Notes Phys., Springer, Cham, 2014).
- [51] Á. Parra-López and J. Bergli, Synchronization in two-level quantum systems, *Phys. Rev. A* **101**, 062104 (2020).
- [52] J. Tindall, C. S. Munoz, B. Buča, and D. Jaksch, Quantum synchronisation enabled by dynamical symmetries and dissipation, *New J. Phys.* **22**, 013026 (2020).
- [53] B. Buča, C. Booker, and D. Jaksch, Algebraic theory of quantum synchronization and limit cycles under dissipation, *SciPost Phys.* **12**, 097 (2022).
- [54] V. Ameri, M. Eghbali-Arani, A. Mari, A. Farace, F. Kheirandish, V. Giovannetti, and R. Fazio, Mutual information as an order parameter for quantum synchronization, *Phys. Rev. A* **91**, 012301 (2015).
- [55] N. Jaseem, M. Hajdušek, P. Solanki, L.-C. Kwek, R. Fazio, and S. Vinjanampathy, Generalized measure of quantum synchronization, *Phys. Rev. Research* **2**, 043287 (2020).
- [56] A. Mari, A. Farace, N. Didier, V. Giovannetti, and

- R. Fazio, Measures of Quantum Synchronization in Continuous Variable Systems, *Phys. Rev. Lett.* **111**, 103605 (2013).
- [57] N. Lörch, J. Qian, A. Clerk, F. Marquardt, and K. Hammerer, Laser theory for optomechanics: Limit cycles in the quantum regime, *Phys. Rev. X* **4**, 011015 (2014).
- [58] T. Weiss, S. Walter, and F. Marquardt, Quantum-coherent phase oscillations in synchronization, *Phys. Rev. A* **95**, 041802 (2017).
- [59] A. Gómez-León and G. Platero, Floquet-Bloch Theory and Topology in Periodically Driven Lattices, *Phys. Rev. Lett.* **110**, 200403 (2013).
- [60] G. Engelhardt, M. Benito, G. Platero, and T. Brandes, Topological instabilities in ac-driven bosonic systems, *Phys. Rev. Lett.* **117**, 045302 (2016).
- [61] M. Bello, C. E. Creffield, and G. Platero, Long-range doublon transfer in a dimer chain induced by topology and ac fields, *Sci. Rep.* **6**, 1 (2016).
- [62] G. Engelhardt, M. Benito, G. Platero, and T. Brandes, Topologically enforced bifurcations in superconducting circuits, *Phys. Rev. Lett.* **118**, 197702 (2017).
- [63] M. Bello, G. Platero, J. I. Cirac, and A. González-Tudela, Unconventional quantum optics in topological waveguide qed, *Sci. Adv.* **5**, eaaw0297 (2019).
- [64] E. Kim, X. Zhang, V. S. Ferreira, J. Banker, J. K. Iverson, A. Sipahigil, M. Bello, A. González-Tudela, M. Mirhosseini, and O. Painter, Quantum electrodynamics in a topological waveguide, *Phys. Rev. X* **11**, 011015 (2021).
- [65] W. Su, J. Schrieffer, and A. J. Heeger, Solitons in polyacetylene, *Phys. Rev. Lett.* **42**, 1698 (1979).
- [66] A. J. Heeger, S. Kivelson, J. Schrieffer, and W.-P. Su, Solitons in conducting polymers, *Rev. Mod. Phys.* **60**, 781 (1988).
- [67] J. K. Asboth, L. Oroszlany, and A. Palyi, *A short course on topological insulators* (Springer, 2015).
- [68] M. Ezawa, Higher-order topological insulators and semimetals on the breathing kagome and pyrochlore lattices, *Phys. Rev. Lett.* **120**, 026801 (2018).
- [69] F. K. Kunst, G. van Miert, and E. J. Bergholtz, Lattice models with exactly solvable topological hinge and corner states, *Phys. Rev. B* **97**, 241405 (2018).
- [70] A. Bolens and N. Nagaosa, Topological states on the breathing kagome lattice, *Phys. Rev. B* **99**, 165141 (2019).
- [71] H. Xue, Y. Yang, F. Gao, Y. Chong, and B. Zhang, Acoustic higher-order topological insulator on a kagome lattice, *Nat. Mater.* **18**, 108 (2019).
- [72] F. Schindler, A. M. Cook, M. G. Vergniory, Z. Wang, S. S. Parkin, B. A. Bernevig, and T. Neupert, Higher-order topological insulators, *Sci. Adv.* **4**, eaat0346 (2018).
- [73] X. Ni, M. Weiner, A. Alu, and A. B. Khanikaev, Observation of higher-order topological acoustic states protected by generalized chiral symmetry, *Nat. Mater.* **18**, 113 (2019).
- [74] D. Leibfried, R. Blatt, C. Monroe, and D. Wineland, Quantum dynamics of single trapped ions, *Rev. Mod. Phys.* **75**, 281 (2003).
- [75] A. Jayich, J. Sankey, B. Zwickl, C. Yang, J. Thompson, S. Girvin, A. Clerk, F. Marquardt, and J. Harris, Dispersive optomechanics: a membrane inside a cavity, *New J. Phys.* **10**, 095008 (2008).
- [76] J. Thompson, B. Zwickl, A. Jayich, F. Marquardt, S. Girvin, and J. Harris, Strong dispersive coupling of a high-finesse cavity to a micromechanical membrane, *Nature* **452**, 72 (2008).
- [77] J. C. Sankey, C. Yang, B. M. Zwickl, A. M. Jayich, and J. G. Harris, Strong and tunable nonlinear optomechanical coupling in a low-loss system, *Nat. Phys.* **6**, 707 (2010).
- [78] M. Aspelmeyer, T. J. Kippenberg, and F. Marquardt, Cavity optomechanics, *Rev. Mod. Phys.* **86**, 1391 (2014).
- [79] A. Nunnenkamp, K. Børkje, J. Harris, and S. Girvin, Cooling and squeezing via quadratic optomechanical coupling, *Phys. Rev. A* **82**, 021806 (2010).
- [80] K. Thornburg, M. Möller, R. Roy, T. Carr, R.-D. Li, and T. Erneux, Chaos and coherence in coupled lasers, *Phys. Rev. E* **55**, 3865 (1997).
- [81] J. J. Lynch and R. A. York, A mode locked array of coupled phase locked loops, *IEEE Microw. Guide Wave Lett.* **5**, 213 (1995).
- [82] A. Cawthorne, P. Barbara, S. Shitov, C. Lobb, K. Wiesenfeld, and A. Zangwill, Synchronized oscillations in josephson junction arrays: The role of distributed coupling, *Phys. Rev. B* **60**, 7575 (1999).
- [83] R. Fazio and H. Van Der Zant, Quantum phase transitions and vortex dynamics in superconducting networks, *Phys. Rep.* **355**, 235 (2001).
- [84] A. Slavin, Spin-torque oscillators get in phase, *Nature Nanotech.* **4**, 479 (2009).
- [85] N. Jaseem, M. Hajdušek, V. Vedral, R. Fazio, L.-C. Kwek, and S. Vinjanampathy, Quantum synchronization in nanoscale heat engines, *Phys. Rev. E* **101**, 020201 (2020).
- [86] T. Nishikawa and A. E. Motter, Comparative analysis of existing models for power-grid synchronization, *New J. Phys.* **17**, 015012 (2015).
- [87] J. C. Bellamy, Digital network synchronization, *IEEE Commun. Mag.* **33**, 70 (1995).
- [88] S. Bregni, Clock stability characterization and measurement in telecommunications, *IEEE Trans. Instrum. Meas.* **46**, 1284 (1997).
- [89] L. Narula and T. E. Humphreys, Requirements for secure clock synchronization, *IEEE J. Sel. Top. Signal Process.* **12**, 749 (2018).
- [90] L. Calderaro, A. Stanco, C. Agnesi, M. Avesani, D. Dequal, P. Villoresi, and G. Vallone, Fast and simple qubit-based synchronization for quantum key distribution, *Phys. Rev. Applied* **13**, 054041 (2020).
- [91] C. Agnesi, M. Avesani, L. Calderaro, A. Stanco, G. Folletto, M. Zahidy, A. Scriminich, F. Vedovato, G. Vallone, and P. Villoresi, Simple quantum key distribution with qubit-based synchronization and a self-compensating polarization encoder, *Optica* **7**, 284 (2020).

## Appendix A: Derivation of the effective quantum model in the comoving frame

In this section we derive the effective master Eq. (13) of the main manuscript governing the dynamics of quantum fluctuations. Our starting point is the master equation (throughout this section we  $\hbar \equiv 1$ )

$$\dot{\rho} = -i[H_S, \rho] + \sum_j \{ \kappa_1 \mathcal{D}[a_j^\dagger] \rho + \kappa_2 \mathcal{D}[a_j^2] \rho \}. \quad (\text{A1})$$

with  $H_S = \omega_0 \sum_j a_j^\dagger a_j + H_{\text{top}}$ . The density matrix in the displaced frame is defined in terms of the displacement operator  $\varrho_\alpha(t) = D^\dagger[\alpha(t)] \varrho(t) D[\alpha(t)]$  with corresponding master equation:

$$\dot{\varrho}_\alpha = -i[\tilde{H}_S, \varrho_\alpha] + \mathcal{L}_1 \varrho_\alpha + \mathcal{L}_2 \varrho_\alpha \quad (\text{A2})$$

where the transformed system Hamiltonian is given by

$$\tilde{H}_S = D^\dagger[\alpha(t)] (H_S - i\partial_t) D[\alpha(t)], \quad (\text{A3})$$

and the two dissipators by

$$\begin{aligned} \mathcal{L}_1 \varrho_\alpha &= \kappa_1 \sum_j D^\dagger[\alpha(t)] \mathcal{D}[a_j^\dagger] \varrho D[\alpha(t)], \\ \mathcal{L}_2 \varrho_\alpha &= \kappa_2 \sum_j D^\dagger[\alpha(t)] \mathcal{D}[a_j^2] \varrho D[\alpha(t)]. \end{aligned} \quad (\text{A4})$$

We now evaluate the effect of applying the displacement operator on the different terms appearing in Eq. (A2). For transformed Hamiltonian  $\tilde{H}_S$  we obtain

$$\begin{aligned} \tilde{H}_S &= \omega_0 \sum_j D^\dagger[\alpha(t)] a_j^\dagger a_j D[\alpha(t)] + D^\dagger[\alpha(t)] H_{\text{top}} D[\alpha(t)] - iD^\dagger[\alpha(t)] \partial_t D[\alpha(t)] \\ &= H_S + H_{\text{top}} + \omega_0 \sum_j \left( \alpha_j a_j^\dagger + \alpha_j^* a_j + |a_j|^2 \right) + \sum_{jj'} \left\{ \lambda_{jj'} (\alpha_j^* a_{j'} + \alpha_{j'} a_j^\dagger + \alpha_j^* a_{j'}) + \lambda_{j'j}^* (\alpha_j^* a_j + \alpha_j a_{j'}^\dagger + \alpha_j^* a_j) \right\} \\ &\quad - i \sum_j \left[ \dot{\alpha}_j \left( a_j^\dagger + \frac{1}{2} \alpha_j^* \right) - \dot{\alpha}_j^* \left( a_j + \frac{1}{2} \alpha_j \right) \right]. \end{aligned} \quad (\text{A5})$$

For the dissipative term proportional to  $\kappa_1$  we obtain

$$\mathcal{L}_1 \varrho_\alpha = \kappa_1 \sum_j D^\dagger[\alpha(t)] \mathcal{D}[a_j^\dagger] \varrho D[\alpha(t)] = \kappa_1 \sum_j \left\{ \mathcal{D}[a_j^\dagger] \varrho_\alpha - i \frac{1}{2} [i\alpha_j a_j^\dagger - i\alpha_j^* a_j, \varrho_\alpha] \right\}, \quad (\text{A6})$$

and for the dissipative term proportional to  $\kappa_2$  we obtain

$$\begin{aligned} \mathcal{L}_2 \varrho_\alpha &= \kappa_2 \sum_j D^\dagger[\alpha(t)] \mathcal{D}[a_j^2] \varrho D[\alpha(t)] \\ &= \kappa_2 \sum_j \left\{ \mathcal{D}[a_j^2] \varrho_\alpha + 4|\alpha_j|^2 \mathcal{D}[a_j] \varrho_\alpha + 2\alpha_j^* \left( a_j^2 \varrho_\alpha a_j^\dagger - \frac{1}{2} a_j^2 a_j^\dagger \varrho_\alpha - \frac{1}{2} \varrho_\alpha a_j^2 a_j^\dagger \right) \right. \\ &\quad \left. + 2\alpha_j \left( a_j \varrho_\alpha (a_j^\dagger)^2 - \frac{1}{2} a_j (a_j^\dagger)^2 \varrho_\alpha - \frac{1}{2} \varrho_\alpha a_j (a_j^\dagger)^2 \right) + \frac{1}{2} [(\alpha_j^*)^2 a_j^2 - \alpha_j^2 (\alpha_j^\dagger)^2, \varrho_\alpha] + |\alpha_j|^2 [\alpha_j^* a_j - \alpha_j a_j^\dagger, \varrho_\alpha] \right\} \\ &= \kappa_2 \sum_j \left\{ 4|\alpha_j|^2 \mathcal{D}[a_j] \varrho_\alpha - i \frac{1}{2} [i(\alpha_j^*)^2 a_j^2 - i\alpha_j^2 (\alpha_j^\dagger)^2, \varrho_\alpha] - i|\alpha_j|^2 [i\alpha_j^* a_j - i\alpha_j a_j^\dagger, \varrho_\alpha] \right\} + \mathcal{O}(a_j^3) \end{aligned} \quad (\text{A7})$$

We now realize that as long as condition (8) i.e., the mean field equation, is satisfied, the linear terms vanish. If we neglect higher order terms, the quantum fluctuations are governed by master equation of Lindblad form:

$$\dot{\varrho}_\alpha = -i[H_\alpha, \varrho_\alpha] + \sum_j \left\{ \kappa_1 \mathcal{D}[a_j^\dagger] \varrho_\alpha + 4\kappa_2 |\alpha_j|^2 \mathcal{D}[a_j] \varrho_\alpha \right\} \quad (\text{A8})$$

with effective Hamiltonian

$$H_\alpha = H_S - i \frac{\kappa_2}{2} \sum_j (\alpha_j^2 a_j^\dagger a_j^\dagger - \alpha_j^* a_j a_j). \quad (\text{A9})$$

## Appendix B: Specific form of the equation governing the covariance matrix

In this section we specify the entries of the matrices  $\underline{\mathbf{B}}$  and  $\underline{\mathbf{D}}$  governing the equation of motion of the covariance matrix  $\underline{\mathbf{C}}$ :

$$\dot{\underline{\mathbf{C}}} = \underline{\mathbf{B}} \underline{\mathbf{C}} + \underline{\mathbf{C}} \underline{\mathbf{B}}^\top + \underline{\mathbf{D}}. \quad (\text{B1})$$

The entries of the matrices are given through Eq. (13). Specifically,  $\underline{\mathbf{B}}$  is a block matrix, where the blocks on the diagonal  $\underline{\mathbf{B}}_{jj}$  take the form

$$\underline{\mathbf{B}}_{jj} = \frac{1}{2} \begin{pmatrix} \kappa_1 - 4\kappa_2 |\alpha_j|^2 - \kappa_2 [(\alpha_j^*)^2 + \alpha_j^2] & -2\omega - i\kappa_2 [(\alpha_j^*)^2 - \alpha_j^2] \\ +2\omega - i\kappa_2 [(\alpha_j^*)^2 - \alpha_j^2] & \kappa_1 - 4\kappa_2 |\alpha_j|^2 + \kappa_2 [(\alpha_j^*)^2 + \alpha_j^2] \end{pmatrix} \quad (\text{B2})$$

and the off-diagonal block matrices  $\underline{\mathbf{B}}_{jk}$  for  $j \neq k$  the form

$$\underline{\mathbf{B}}_{jj'} = \lambda_{jj'} \begin{pmatrix} 0 & 1 \\ -1 & 0 \end{pmatrix}. \quad (\text{B3})$$

Furthermore,  $\underline{\mathbf{D}}$  is a diagonal block matrix with entries  $\underline{\mathbf{D}}_{jj}$  on the diagonal given by

$$\underline{\mathbf{D}}_{jj} = \frac{1}{2} (\kappa_1 + 4\kappa_2 |\alpha_j|^2) \begin{pmatrix} 1 & 0 \\ 0 & 1 \end{pmatrix}. \quad (\text{B4})$$

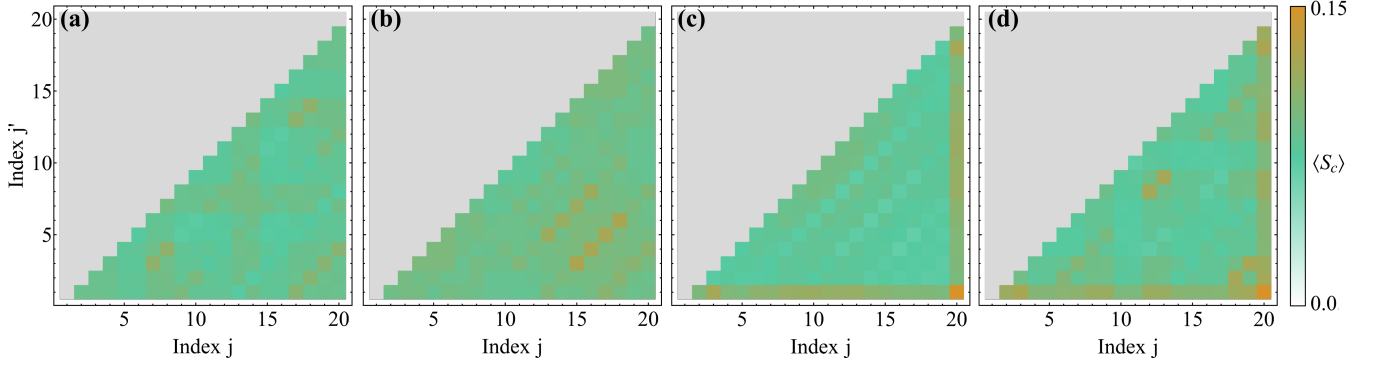


FIG. 13. Time-averaged quantum complete synchronization measure  $\langle S_c \rangle$  between lattice site  $j$  and  $j'$  of the vdP SSH network corresponding to the mean field dynamics shown in Fig. 2, i.e., with an eigenstate  $\alpha^{(l)}$  of the topological Hamiltonian  $H_{SSH}$  [cf. Eq. (16)] as initial conditions and for different coupling strength (a)  $\delta\lambda = -0.8\lambda_0$ , (b)  $\delta\lambda = -0.4\lambda_0$ , (c)  $\delta\lambda = 0.4t_0$ , and (d)  $\delta\lambda = 0.6\lambda_0$ . With an eigenstate as initial state, additional structures emerge compared to random initial conditions. Nevertheless,  $\langle S_c \rangle$  between the edges ( $j' = 1$  and  $j = 20$ ) is still the largest quantity. Parameters:  $\kappa_1 = 5 \cdot 10^{-3}\omega_0$ ,  $\kappa_2 = 2\kappa_1$ ,  $\lambda_2 = 0.25\omega_0$ ,  $\omega_0 t_i = 2 \cdot 10^4$ ,  $\omega_0 t_f = 2.3 \cdot 10^4$ .

### Appendix C: Quantum signatures in the SSH model for eigenstates as initial conditions

In this section we provide for completeness the quantum synchronization measure  $\langle S_c \rangle$  corresponding to the mean field amplitudes shown in Fig. 2, that is we choose eigenstates  $\alpha^{(l)}$  of the topological Hamiltonian  $H_{SSH}$  [cf. Eq. (16)] as initial states (cf. Sec. III B 2). In Figs. 13(a)-(d) we show the time-averaged quantity  $\langle S_c \rangle$  between lattice site  $j$  and  $j'$  of the vdP chain for different coupling strengths (a)  $\delta\lambda = -0.8\lambda_0$ , (b)  $\delta\lambda = -0.4\lambda_0$ , (c)  $\delta\lambda = 0.4t_0$ , and (d)  $\delta\lambda = 0.6\lambda_0$ . In the trivial phase we observe complete synchronization of all vdP oscillators for the mean fields shown in Figs. 2(b) and (c) with oscillation amplitudes determined by the amplitudes of the initial state. Moreover, the amplitudes are symmetric with symmetry center located in the middle of the chain, i.e. between oscillator  $j = 10$  and  $j = 11$ . For the quantum model, this symmetry is reflected in the synchronization measure shown in Figs. 13(a) and (b), i.e.,  $\langle S_c(j', j) \rangle = \langle S_c(j' = N + 1 - j, j = N + 1 - j') \rangle$ , for example  $\langle S_c(j' = 3, j = 7) \rangle = \langle S_c(j' = 14, j = 18) \rangle$  in Fig. 13(a). However, besides this observation, comparing the mean field dynamics with the emergent quantum synchronization remains challenging and will be investigated further in future work.

The bulk oscillators in the topological phase shown in Figs. 13(b) and (c) corresponding to the mean field amplitudes of Figs. 2(d) and (e), respectively, exhibit similar behavior as discussed previously; notably  $\langle S_c(j', j) \rangle$  reflects the symmetry of the system. However, in addition the oscillators located at the two edges of the chain ( $j' = 1$  and  $j = 20$ ) exhibit the largest value of the quantum synchronization measure in the vdP chain. It is worth mentioning that the oscillators located at the boundaries live on different sublattices ( $j' = 1$  is odd and  $j = 20$  is even)

and furthermore exhibit in-phase synchronization of the mean field amplitudes; see Figs. 2(d) and (e).

### Appendix D: Including an additional linear loss channel

For the experimental realization of a vdP oscillator with optomechanics as discussed in Sec. V, there exists an additional linear one-phonon loss channel. However, we will show in this section that such an additional dissipative term does not affect the results discussed in the main text as long as it is small compared to the linear gain channel. Including this additional loss term, the Lindblad master equation is given by

$$\dot{\rho} = -\frac{i}{\hbar} [H, \rho] + \sum_j \left\{ \kappa_1 \mathcal{D}[a_j^\dagger] \rho + \kappa_2 \mathcal{D}[a_j^2] \rho + \bar{\gamma} \mathcal{D}[a_j^\dagger] \rho \right\}. \quad (D1)$$

Within in the mean field approximation, the term proportional to  $\bar{\gamma}$  only appears as a shift of the dissipation rate  $\kappa_1$ , i.e., with the definition  $\tilde{\kappa}_1 = \kappa_1 - \bar{\gamma}$  the dynamics is fully equivalent to Eq.(13) assuming that  $\bar{\gamma} \ll \kappa_1$ . The latter condition must be fulfilled in order to counteract the nonlinear damping ( $\kappa_2$ ) and not simply decay into the ground state.

In terms of the quantum fluctuations about these mean field amplitudes, the additional  $\bar{\gamma}$  term appears in the matrices  $\underline{B}$  and  $\underline{D}$  governing the dynamics of the covariance matrix; see Eq. (15). Similar to the mean field approximation, in  $\underline{B}$  this will only result in an effective dissipation rate  $\kappa_1 \rightarrow \tilde{\kappa}_1 = \kappa_1 - \bar{\gamma}$  in Eq. (B2). However, the sign is flipped for the effective dissipation rate in  $\underline{D}$  [cf. Eq. (B4)], which is then given by

$$\underline{D}_{jj} = \frac{1}{2} (\kappa_1 + \bar{\gamma} + 4\kappa_2 |\alpha_j|^2) \begin{pmatrix} 1 & 0 \\ 0 & 1 \end{pmatrix}. \quad (D2)$$

We have checked numerically that for  $\bar{\gamma} = 0.1\kappa_1$  there are no noticeable changes in the dynamics or synchronization

behavior, such that we are confident that in fact a linear dissipation channel does not alter the discussed results.